



HAL
open science

Characteristics of Saturn's FUV airglow from limb viewing spectra obtained with Cassini-UVIS

Jacques Gustin, Ian Stewart, Jean-Claude Gérard, Larry Esposito

► **To cite this version:**

Jacques Gustin, Ian Stewart, Jean-Claude Gérard, Larry Esposito. Characteristics of Saturn's FUV airglow from limb viewing spectra obtained with Cassini-UVIS. *Icarus*, 2010, 210 (1), pp.270. 10.1016/j.icarus.2010.06.031 . hal-00683835

HAL Id: hal-00683835

<https://hal.science/hal-00683835>

Submitted on 30 Mar 2012

HAL is a multi-disciplinary open access archive for the deposit and dissemination of scientific research documents, whether they are published or not. The documents may come from teaching and research institutions in France or abroad, or from public or private research centers.

L'archive ouverte pluridisciplinaire **HAL**, est destinée au dépôt et à la diffusion de documents scientifiques de niveau recherche, publiés ou non, émanant des établissements d'enseignement et de recherche français ou étrangers, des laboratoires publics ou privés.

Accepted Manuscript

Characteristics of Saturn's FUV airglow from limb viewing spectra obtained with Cassini-UVIS

Jacques Gustin, Ian Stewart, Jean-Claude Gérard, Larry Esposito

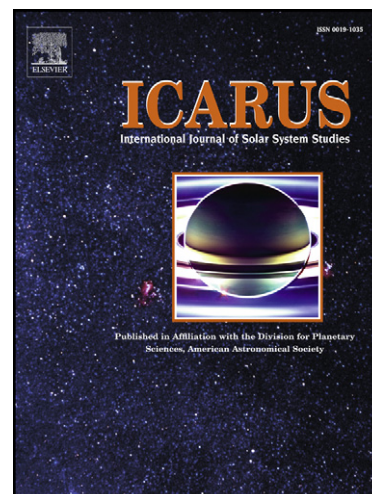
PII: S0019-1035(10)00253-8
DOI: [10.1016/j.icarus.2010.06.031](https://doi.org/10.1016/j.icarus.2010.06.031)
Reference: YICAR 9483

To appear in: *Icarus*

Received Date: 1 December 2009
Revised Date: 11 June 2010
Accepted Date: 21 June 2010

Please cite this article as: Gustin, J., Stewart, I., Gérard, J-C., Esposito, L., Characteristics of Saturn's FUV airglow from limb viewing spectra obtained with Cassini-UVIS, *Icarus* (2010), doi: [10.1016/j.icarus.2010.06.031](https://doi.org/10.1016/j.icarus.2010.06.031)

This is a PDF file of an unedited manuscript that has been accepted for publication. As a service to our customers we are providing this early version of the manuscript. The manuscript will undergo copyediting, typesetting, and review of the resulting proof before it is published in its final form. Please note that during the production process errors may be discovered which could affect the content, and all legal disclaimers that apply to the journal pertain.



1 **Characteristics of Saturn's FUV airglow from limb**
2 **viewing spectra obtained with Cassini-UVIS**

3
4 Jacques Gustin^(1,2), Ian Stewart⁽²⁾, Jean-Claude Gérard⁽¹⁾ and Larry Esposito⁽²⁾

5
6 (1) Laboratoire de Physique Atmosphérique et Planétaire, Université de Liège, 4000
7 Liège, Belgium

8 (2) Laboratory for Atmospheric and Space Physics, University of Colorado, Boulder, CO
9 80303, USA

10
11
12
13
14 Submitted to Icarus,

15 Revised version, June 2010

16
17 Manuscript pages: 50

18 Figures: 10

19 Tables: 2

20 **Running head:** UV spectroscopy of Saturn's airglow with Cassini/UVIS

21

22 **Corresponding author:** Jacques Gustin, Laboratoire de Physique Atmosphérique et
23 planétaire, allée du 6 août, 17, 4000 Liège, Belgium.

24 E-mail : gustin@astro.ulg.ac.be

25 Phone: +32 4 366 9796 ; Fax: +32 4 366 9711

26 **Co-authors e-mails:**

27 I. Stewart: Ian.Stewart@lasp.colorado.edu

28 L. Esposito: Larry.Esposito@lasp.colorado.edu

29 J.-C. Gérard: JC.Gerard@ulg.ac.be

30

ACCEPTED MANUSCRIPT

31

32 **Abstract**

33

34 This study reports the analysis of far ultraviolet (FUV) limb spectra of the airglow of
35 Saturn in the 1150-1850 Å spectral window, obtained with the Ultraviolet Imaging
36 Spectrograph (UVIS) onboard Cassini, spanning altitudes from -1200 to 4000 km. The FUV
37 limb emission consists of three main contributions: 1) H Ly- α peaking at 1100 km with a
38 brightness of 0.8 kilo-Rayleighs (kR), 2) reflected sunlight longward of 1550 Å which
39 maximizes at -950 km with 16.5 kR and 3) H₂ bands in the 1150-1650 Å bandwidth, peaking
40 at 1050 km reaching a maximum of 3.9 kR.

41 A vertical profile of the local H₂ volume emission rate has been derived using the
42 hydrocarbon density profiles from a model of the Saturn equatorial atmosphere. It is well
43 matched by a Chapman function, characterized by a maximum value of 3.5 photons cm⁻³ s⁻¹ in
44 the 800-1650 Å UV bandwidth, peaking at 1020 km.

45 Comparisons between the observed spectra and a first order synthetic airglow H₂
46 model in the 1150-1650 Å bandwidth show that the spectral shape of the H₂ bands is
47 accounted for by solar fluorescence and photoelectron excitation. The best fits are obtained
48 with a combination of H₂ fluorescence lines and 20 eV electron impact spectra, the latter
49 contributing ~68% of the total H₂ airglow emission.

50

51

52 **Keywords:** airglow, Saturn, spectroscopy, ultraviolet observations

53

54

55

56 **1. Introduction**

57

58 The first observations of Saturn's ultraviolet (UV) emissions were obtained by the
 59 Voyager encounters in the early eighties. Comparisons between the emissions at Jupiter and
 60 Saturn showed that they are qualitatively similar (Broadfoot *et al.* 1981). The most intense
 61 emission at Saturn detected by the ultraviolet spectrometer (UVS) onboard Voyager 1 (V1)
 62 was the aurora, with ~10 kilo Rayleighs (kR) for both the Hydrogen Lyman α (Ly- α) and the
 63 H₂ bands, followed by dayside Ly- α with ~ 1.5 kR and H₂ dayglow with ~0.7 kR in the
 64 Lyman and Werner bands (Broadfoot *et al.* 1981). The latter value is four times lower than
 65 the Jupiter value, consistent with the factor of ~3 reduction in the solar flux from Jupiter to
 66 Saturn. This fact, among others, pleaded for a dayglow stimulated by the solar flux. Several
 67 UVS spectra were examined by Shemansky and Ajello (1983). They compared the observed
 68 dayside H₂ bands with electron-excited synthetic spectra that includes the $B^1\Sigma_u^+$,
 69 $E, F^1\Sigma_g^+, C^1\Pi_u, B^1\Sigma_u^+, D^1\Pi_u, B^1\Sigma_u^+$, and $D^1\Pi_u$ to $X^1\Sigma_g^+$ vibronic transitions and
 70 confirmed that, as for Jupiter, H₂ emission from electronic collisions makes a significant
 71 contribution to the observed UV intensity. They also pointed out that the emission longward
 72 of 1500 Å is dominated by reflection of solar radiation. Although the electron impact
 73 excitation and the solar flux control suggest that the H₂ dayglow is produced by
 74 photoelectrons, this idea has been, at first, partially rejected for energy budget considerations
 75 (Broadfoot *et al.* 1981). Precipitation of magnetospheric electrons has been proposed several
 76 times (Strobel, 1979, Chen, 1981), but never been considered as an appropriate mechanism to
 77 account for the various features of the dayglow phenomenon.

78 As for Jupiter and Saturn, the dayglow observed after the Voyager Uranus encounter
 79 was found to exceed the available photoelectron energy, assuming that 15% of the total solar
 80 EUV energy goes into photoelectron excitation of FUV emission (Cravens *et al.* 1975). A

81 process called “electroglow” was proposed by Broadfoot *et al.* (1986). As many UVS
82 dayglow spectra were well fit by electron excitation models, it was considered that
83 electroglow consisted of soft (~50 eV) charged particle excitation in the presence of sunlight.
84 Since the dayglow demonstrated correlation with solar zenith angle and the heliocentric
85 scaling, it was supposed that electroglow was completely controlled by the incident solar flux
86 (Yelle *et al.* 1987). Several mechanisms were considered. For example, Yelle *et al.* (1987)
87 proposed that electroglow was produced by fluorescence or H⁺ photolysis. Since electroglow
88 was created to explain the emission in excess of available solar energy, Clarke *et al.* (1987)
89 objected that electroglow was not a direct consequence of solar input, but produced by in-situ
90 electric field acceleration of photoelectrons and ions through an atmospheric dynamo. This
91 mechanism was neither satisfactory, as it should have a strong dependence of magnetic
92 coordinates, which was not observed. Yelle, (1988) suggested that solar fluorescence could
93 significantly contribute to the observed outer planet dayglows. He built two independent
94 models of H₂ emission, excited by photoelectrons and solar fluorescence, and first pointed out
95 significant differences between the emission due to the two excitation sources: the electron-
96 excited spectrum consists of a large number of vibronic transitions distributed relatively
97 smoothly with wavelength, while the solar fluorescence H₂ spectrum mainly consists of a
98 series of bright emission lines produced by the absorption and reradiation of solar lines into
99 H₂ bands. Using a combination of photoelectron-excited and solar fluorescence-excited
100 spectra, he was able to obtain a good fit to a Jovian Voyager UVS spectrum without the need
101 for additional sources. As the Saturn UVS spectra appear very similar to that of Jupiter, he
102 also predicted that Saturn’s dayglow emission could be accounted for by a combination of
103 fluorescence and photoelectron excitations. He however indicated that his simple model
104 suffered from substantial uncertainty. Combined with the uncertainties in the solar flux he
105 used, UVS calibrations, and low UVS spectral resolution (~30Å), he was not able to

106 determine the respective contribution of fluorescence and photoelectron and univocally state
107 that fluorescence and photoelectron excitations can account for the total observed brightness.

108 This controversy was finally cleared out by Liu and Dalgarno, (1996), who compared
109 a ~ 3 Å resolution Jovian dayglow spectrum obtained by the Hopkins Ultraviolet Telescope
110 (HUT) at solar maximum with a self-consistent model of the airglow of H₂, excited by the
111 absorption of solar EUV radiation. The much higher spectral resolution of HUT spectra (than
112 UVS) and more accurate calibrations provided a very convincing demonstration that solar
113 fluorescence and photoelectron excitation could explain the H₂ dayglow emissions. Their
114 model took into account the absorption of EUV solar radiation < 500 Å, which ionizes H, H₂
115 and HD, producing an energy spectrum of photoelectron flux, exciting UV H₂ bands by
116 collision, as described in Shemansky and Ajello (1983). The fluorescence part of the UV
117 emission is produced by the strong wavelength coincidences between solar emission lines and
118 absorption lines of H₂ in the 900-1100 Å bandwidth. They found that the UV spectrum of the
119 Jovian dayglow can be accounted for in both brightness and spectral shape by solar
120 fluorescence and photoelectron excitation, without other energy source. In particular, Fig. 3 of
121 Liu and Dalgarno (1996) shows that the majority of photoelectrons producing the UV photons
122 are confined below 60 eV, with a maximum flux at 25 eV and an average energy of 33 eV.
123 These values lie near the maximum of the excitation cross-section of the EF cascade (~ 20 eV)
124 and B, C (~ 40 eV) (Ajello *et al.* 1982). With a maximum flux at 25 eV, it is likely that the
125 cascade process which populates the $B^1\Sigma_u^+$ electronic state through $E, F^1\Sigma_g^+$, has a important
126 contribution in the photoelectron-excited spectrum. This point was raised by Prangé (1986),
127 who observed a small peak near 1300 Å in a low resolution V1 UVS Saturn's disk spectrum,
128 which may indicate a enhancement of EF cascade in the dayglow emission compared to the
129 aurora. Liu and Dalgarno (1996) estimated solar fluorescence to contribute 57% to the total
130 2.3 kR of the Jovian dayglow HUT spectrum. Since the airglow brightness depends on solar

131 conditions and gas temperature, these values may not be readily applied to our Saturn
132 observations. Yet, the work by Liu and Dalgarno (1996) gives a good overview of the
133 processes responsible to the observed dayglow UV emissions.

134 The Saturn limb profiles from V1 and Voyager 2 (V2) have been re-analyzed by Yelle
135 *et al.* (1986). At that time, the source of the UV dayglow emission was still controversial, but
136 some interesting conclusions should be emphasized. First, they noticed that the limb profile of
137 Ly- α and H₂ band peaked at about the same altitude, near the homopause, at ~60000 km
138 minimum ray height (MRH) for the V2 limb drift. As they assigned the 1 bar level at ~59000
139 km, it situates the H₂ emission near 1000 km above the 1 bar level. The uncertainty is
140 determined by the slit width, which was ~400 km. The line of sight (LOS) measurements
141 must be inverted to yield the emission rate variation with altitude. Yelle *et al.* (1986) used a
142 forward technique, consisting of modeling the volume emission rate (VER) and adjusting the
143 model to get the best fit to the observed limb profile. Using the CH₄ densities from Smith *et*
144 *al.* (1983) to take into account the extinction due to methane, their best VER was a
145 combination of two exponentials. A first one with a scale height of 1500 km, which best fit
146 the observed brightness above 60500 km and a second one with a scale height of 200 km, best
147 fitting the observed brightness below 60500 km. This vertical VER produced ~ 2 photons cm⁻²
148 s⁻¹ at the merging 60500 km. As the scale heights they used is from five to ten times the
149 ambient gas value from Smith *et al.* (1983), Yelle *et al.* (1986) concluded that the airglow
150 emission was present throughout the entire thermosphere. They also mentioned that similar
151 results had been achieved with an inversion technique calculations.

152 In terms of composition, a first model of Saturn's upper atmosphere has been derived
153 by Smith *et al.* (1983) from the analysis of V2 UVS occultation measurements, providing
154 temperature and H, H₂ and CH₄ density profiles. Until recently, most of the Saturn's
155 photochemical models were based on photochemical processes operating on Jupiter and

156 extrapolated to Saturn. The first comprehensive model of Saturn's atmosphere was published
157 by Moses *et al.* (2000). It used the latest hydrocarbon reaction rates, absorption cross sections,
158 and photolysis quantum yields as well as observational constraints from infrared to
159 ultraviolet. As for Jupiter, they found that the main hydrocarbons are CH₄, C₂H₆ and C₂H₂, in
160 that order of abundance.

161 In this study, we analyze limb-viewing spectra of Saturn obtained with the UltraViolet
162 Imaging Spectrograph (UVIS) onboard Cassini, obtained at a continuous set of MRH
163 altitudes. In contrast to Voyager UVS limb observations, obtained at ~30 Å spectral resolution
164 with a spatial resolution of ~400 km, UVIS provides high signal to noise spectra at ~5.5 Å
165 resolution with a spatial resolution of ~300 km. The goal of this paper is to 1) derive the
166 vertical VER of the H₂ dayglow, taking into account the absorbing hydrocarbons attenuating
167 the signal along the LOS, 2) provide a spectral analysis of the FUV airglow limb spectra and
168 3) establish limb profiles of the sources of the observed emissions.

169 **2. Observations and data reduction**

170

171 The data examined here consist of six sets of observations listed in Table 1. The first
172 two sets were collected on 29 October 2005 and the other four ones on 27 November 2005,
173 i.e. near solar minimum. Fig. 1a shows the projection of the UVIS FUV slit near Saturn's disk
174 for the first set and Fig. 1b gives a general outlook of the viewing geometry. The UVIS
175 instrument has been thoroughly described by Esposito *et al.* (2004). In brief, UVIS includes a
176 two-channel imaging spectrograph, from 1115 to 1912 Å in the FUV, and from 563 to 1182 Å
177 in the EUV. Three slits are available: a high resolution slit (75 and 100 µm slit width for the
178 FUV and EUV channel, respectively), a low resolution slit (150 and 200 µm slit width for the
179 FUV and EUV respectively), and an occultation slit of 800 µm width, identical for both
180 channels. The data discussed here were obtained with the low resolution slit and FUV
181 channels, providing spectra at ~5.5 Å spectral resolution. The detector is a Codacon (CODed
182 Anode array CONverter), consisting of 1024 pixels in the spectral direction and 64 pixels in
183 the spatial direction. The spectral dimension was compressed by two pixels throughout the
184 observation sequences to reduce data volume. The distance between Cassini and Saturn at the
185 tangent point varied from 2.7×10^5 to 3.0×10^5 km, leading to a spatial resolution of about
186 300 km per pixel, assuming a spatial pixel field of view of 1.0 mrad. The average phase and
187 incidence angles of all spatial pixels at the tangent point along the LOS are 96.0 and 24.7
188 degrees respectively, with a constant emission angle of 90 degrees.

189 Taking into account the illuminated spatial pixels only (56 pixels for all observations
190 except observation number two which has 57), the dataset consists of 14133 spectra. The first
191 step of the reduction process is to sort all the spectra by MRH and add them up into bins of 50
192 km, in order to examine the dayglow variations with altitude. This procedure has been applied
193 by Stevens *et al.* (2010) in the analysis of Titan's UVIS limb spectra. Assigning the central

194 altitude value for each 50 km bin, we obtain a total of 109 spectra, spanning a continuous
195 altitude range from -1325 to 4125 km MRH. Negative values of the MRH correspond to
196 altitudes where the tangent point of the line of sight is situated below the 1 bar level. The
197 spectra are then calibrated, using a procedure already applied to other UVIS analysis (Ajello
198 *et al.* 2008, Gustin *et al.* 2009, Stevens *et al.* 2010). It consists in a subtraction of the
199 background noise due to the radioisotope thermoelectric generator onboard Cassini, a flat-
200 field correction, and conversion from counts to Rayleigh \AA^{-1} using the time-dependent
201 sensitivity curve prescribed by the UVIS team. The last three high-altitude spectra at 4025,
202 4075 and 4125 km have been used as background reference and have been subtracted from all
203 spectra. Another source of background signal that affects the recorded spectra is scattering of
204 the H Ly- α line on the detector. This wavelength-dependent background, directly proportional
205 to the Ly- α intensity, has been modeled, scaled to the observed Ly- α and subtracted from the
206 data. Fig 2a shows the variations of the spectral contents and intensity for several altitude
207 bins. It is seen that a strong solar reflectance structure longward of 1500 \AA dominates the
208 overall intensity for lower altitude spectra (~ -1325 to ~ 425 km) and spectra above ~ 425 km
209 contain strong H₂ Lyman and Werner bands. Limb spectra above 2700 km start to be very
210 noisy and structureless. Fig. 2b shows the brightness variations of the reflected sunlight
211 emission in 1700 - 1880 \AA , plus the 1250 - 1300 and 1550 - 1620 \AA spectral windows, used to
212 define the H₂ color ratio (CR), which is a measure of the absorption by methane (Gustin *et al.*
213 2004). The limb reflected solar profile has a maximum of 16.5 kR, peaking at ~ -1075 km. The
214 1230 - 1300 and 1550 - 1620 \AA profiles exhibit the same trend at high altitude up to 1100 km,
215 where the 1250 - 1300 \AA brightness starts to reveal the effect of methane absorption, active
216 shortward of 1400 \AA . The integrated limb brightness in 1550 - 1620 \AA peaks near ~ 825 km and
217 1230 - 1300 \AA one peaks near ~ 975 km. The altitudes scale used in Fig. 2a and 2b is provided
218 by the nominal pointing in the NAIF SPICE C kernel toolkit. It will be demonstrated later that

219 an upward offset of 125 km will be applied to the altitude scale in order to obtain better
220 agreement between the data and model.

ACCEPTED MANUSCRIPT

221 **3. FUV solar reflectivity**

222

223 The main goal of the study is to describe the characteristics of the H₂ dayglow.
224 Between -1325 and 775 km, the spectra in the 1500-1650 Å bandwidth are a combination of
225 the H₂ bands and reflected sunlight. The first natural step is to model the reflected sunlight
226 emission in order to separate the two contributions. The reflected emission is the result of the
227 solar radiation scattering by atmospheric H₂ and He and absorption by the hydrocarbons along
228 the photon trajectory. First, we calculate Saturn's FUV reflectivity in the 1500-1880 Å
229 window using a procedure previously applied by Ajello *et al.* (2008), based on a multiple
230 scattering formalism designed for limb-viewing geometry (Wallach and Hapke, 1985). Each
231 spectrum we analyze is the sum of all spatial pixels into 50 km MRH bins. Since the solar
232 incidence and phase angles can be very different for each pixel into a 50 km bin, we
233 calculated the reflectivity for each individual pixel and then computed a weighted averaged
234 reflectivity, based on each pixel intensity between 1700 and 1880 Å. The modeled reflectivity
235 so calculated is then multiplied by a solar spectrum which accounts for the angle between
236 Saturn, the Sun and the Earth to correct for the solar rotation and the resulting delay between
237 the solar photon flux reaching the Earth and Saturn. The solar flux is then corrected for the
238 distance between the Sun and Saturn. Since the datasets have been obtained 29 days apart,
239 two solar spectra should be considered. We retrieved solar spectra obtained from the
240 TIMED/SEE database (Woods *et al.* 2005), measured on 21 October 2005 and 22 November
241 2005, related to the 29 Oct. 2005 and 27 Nov. 2005 limb observations respectively. As both
242 spectra were found identical, we chose the 21 Oct. 2005 spectrum in our calculations.
243 Because of the limb-viewing geometry, the path crossed by the light is much larger than for
244 disk observations. Therefore we chose to include in the modeled reflectivity, in addition to
245 C₂H₂ and C₂H₆, nine minor hydrocarbons which may have an effect on the total attenuation:

246 C_2H_4 , C_3H_6 , CH_2CCH_2 , C_4H_2 , C_4H_8 , CH_3C_2H , C_3H_8 , C_4H_8 and C_4H_{10} . Since this high number
247 of parameter may lead to unstable results, we chose to tie some hydrocarbon mixing ratios to
248 others. We first choose the hydrocarbons whose number density altitude profiles follow the
249 same trend in the Moses *et al.* (2000) model and tied them to the most abundant one, which
250 can vary freely. In our selection of hydrocarbons, C_2H_2 and C_2H_4 vary freely, C_3H_6 ,
251 CH_2CCH_2 , C_4H_2 and C_4H_8 are tied to CH_3C_2H , and C_3H_8 and C_4H_{10} are tied to C_2H_6 . The
252 average abundance ratios between the “free” and “tied” hydrocarbons along the vertical
253 profile are used to relate the tied hydrocarbons to the free ones. After multiple tests, we added
254 C_6H_6 in the model, whose important absorption cross-section near 1780 Å improved the fit.
255 Since the H_2 emission significantly contributes in the 1500-1650 Å bandwidth, we also
256 included in the regression a synthetic H_2 airglow spectrum in that spectral region as a free
257 parameter. This synthetic H_2 spectrum, provided by J. T. Hallet (personal communication,
258 from Hallet *et al.*, 2005), is described in more details in section 4.1.a. It is used in the present
259 paragraph as an all-around airglow spectrum simulating the influence of H_2 within the
260 reflected sunlight signal. It will be the base of our VER determination presented in section 4.1
261 and 4.2. A least-square fit between the observed and modeled spectra in 1500-1880 Å
262 minimizing chi squares (χ^2) is then applied, yielding the best parameters, which are the
263 mixing ratios of the absorbing components and the scale factor of the synthetic H_2 spectrum.
264 Two examples of fits are shown in Fig. 3, illustrating the strong variation of the H_2
265 contributions compared to reflected sunlight in the 1500-1700 Å spectral region. Figure 4
266 shows the C_2H_2 and C_2H_6 mixing ratios of the best fits for the low altitude spectra up to the
267 1×10^4 mbar level (~800km) along with the Moses *et al.* (2000) values and other published
268 measurements. The Moses *et al.* (2000) profiles show the mixing ratios averaged along the
269 LOS. Data points from disk viewing observations obtained by other studies are also shown.
270 The UVIS C_2H_2 profiles below ~1 mbar and C_2H_6 below $\sim 1 \times 10^{-2}$ mbar do not exhibit a strong

271 altitude dependence. This is an effect of the limb-viewing geometry, which averages the
272 hydrocarbon local density profiles along the LOS and smoothes their variations with the
273 MRH. It should be noted that the UVIS values reflect, for a given MRH, the product of the
274 local solar illumination by the optical depth, summed on each point along the LOS. Therefore,
275 they cannot be readily compared with other published values, since the unattenuated vertical
276 profile of the solar flux is not known, which make it unfeasible to simulate the average
277 mixing ratios that would be obtained in limb-viewing geometry. This is not essential to our
278 analysis, since our goal is to subtract the modeled reflected sunlight component from the
279 observed spectra in order to get the H₂ emission free of solar contamination. Once a best
280 synthetic spectrum is obtained for each MRH, the solar reflected component is then removed
281 from the observations to retain the airglow H₂ emission only.

282 **4. Spectral Analysis**

283

284 4.1. Overview

285 The emergent brightness B at Z_0 MRH is the sum of the H_2 emission on each point S
 286 along the LOS, attenuated by hydrocarbons (Fig. 1b):

287

$$288 \quad B(Z_0) = \int_{-\infty}^{+\infty} v(S) e^{-\tau(S)} dS \quad (1) \quad \text{with}$$

289

$$290 \quad \tau(S) = \int_s^{+\infty} n_{HC}(S') \sigma_{HC} dS' \quad (2) \quad \text{where}$$

291

292 - $v(S)$ is the vertical VER of the H_2 airglow intercepted at distance S along the LOS

293 - $\tau(S)$ is the optical depth due to absorption by hydrocarbon HC, of density n_{HC} at S'

294 and absorption cross-section σ_{HC} .

295 The VER and hydrocarbon density profiles are unknown a-priori. Since they both
 296 significantly influence the emergent signal and are independent unknowns, we chose to fix the

297 vertical hydrocarbon density profiles by using the values from the Moses *et al.* (2000) model.

298 To determine the VER, we evaluate equations (1) and (2) using the Moses *et al.* (2000)

299 atmospheric model, with a Chapman-type function to model the vertical VER:

300

$$301 \quad v = v_m \exp\{f(1 - \alpha - e^{-\alpha})\} \quad (3) \quad \text{where}$$

302

303 - $\alpha = (Z - Z_m)/H$ is the reduced height,

304 - v_m is the maximum of v at the altitude Z_m ,

305 - f is the shape factor, defining a α -Chapman when $f=0.5$ and a β -Chapman when $f=1$.

306 - H determines the thickness of the emission profile. In the case of a β -Chapman profile,

307 H is the scale height of the emission, i.e. the height range in which the topside VER changes

308 by a factor of e (~ 2.718). The β -Chapman is chosen a-priori in our study.

309 We adopt the following steps in the spectral analysis:

310 a. Determination of the VER

311 Using equations (1), (2), (3), the parameters of the Chapman function are derived from

312 a least-squares fit between the calculated and observed profile of $B(Z_0)$ in the integrated 1550-

313 1620 Å spectral window. We chose this bandwidth to avoid the effects of CH_4 , the most

314 abundant hydrocarbon, which has a strong absorption cross-section shortward of 1400 Å.

315 Nevertheless, simulations have shown that the 1550-1620 Å range is not free of absorption

316 because of the long path along the LOS. The optical depth in the model thus includes all the

317 hydrocarbon species used in paragraph 3, with C_2H_2 and C_2H_6 as the stronger absorbers in this

318 spectral band. To account for the wavelength dependence and spectral shape, we incorporate

319 in the model the synthetic spectrum of Saturn's airglow as described by Hallet *et al.* (2005).

320 This H_2 synthetic spectrum is composed of transitions due to both direct excitation by

321 photoelectron and solar photon of the X ground electronic state to B, C, B', D, B'', D' states,

322 and cascade from the excited singlet-gerade states EF, GK, HH, I and J. It uses solar

323 conditions of April 2005 with incidence and emission angles set at 0 deg. This synthetic

324 spectrum is normalized in the 1550-1620 Å bandwidth, multiplied on each point S along the

325 LOS by the intercepted VER, and attenuated by $\tau(S)$. The model uses 10 km steps along the

326 LOS, from -30000 to 30000 km and altitude bins of 50 km MRH from -115 km (minimum

327 altitude tabulated in the Moses *et al.* (2000) model) to 3025 km, where the dayglow tends to

328 zero. The resulting 1550-1620 Å brightness profile is compared to the data and the best fit

329 provides the best parameters of the Chapman function.

330

331 b. Spectral comparison

332 From the best VER determined in a) from the 1550-1620 Å brightness profile, we
333 calculate for each altitude bin an emergent synthetic spectrum in the 1150-1650 Å bandwidth,
334 with the CH₄ profile from Moses *et al.* (2000) added back to the procedure. The VER has
335 been adapted to this wider spectral range by multiplying the best v_m parameter by 4.0. At this
336 stage, a line-by-line comparison between the synthetic and observed spectra is not practical
337 because we have to consider a hundred of spectra. A good way to evaluate the quality of the
338 modeled emergent spectra (and thus the VER and density profiles used in the previous step) is
339 to compare the observed and synthetic CR. This brings a overall view on the ratio between
340 two bandpasses of the spectra and on the CH₄ absorption. If the synthetic CR profile is not
341 satisfactory, the procedure in step a) is performed again, with modified hydrocarbon profiles
342 and/or VER. Once a satisfactory CR profile is obtained, the observed and modeled spectral
343 shape in the 1150-1650 Å are compared to possibly make further adjustments. For example,
344 the examination of the absorption at 1520 Å gives an information on the quantity of C₂H₂ and
345 may allows a fine-tuning of the model.

346 c. Photoelectrons and fluorescence contributions

347 In order to estimate the proportion between the emission due to photoelectrons and
348 solar pumping contributing to the airglow, the synthetic spectrum by Hallet *et al.* (2005) is
349 replaced in paragraph 4.3. by an electron-impact H₂ laboratory spectrum, associated with
350 individual H₂ fluorescence lines found in Table 2 of Liu and Dalgarno, (1996). The best fit
351 between the observed and modeled emergent spectra provides a first estimate of the
352 contribution of each excitation process.

353

354 4.2. Volume emission rate

355

356 Applying the procedure described in 4.1., the first synthetic CR profile we derived was
357 too high and did not match the observed one at all (see the orange curve with diamonds in
358 Fig. 7). A natural way to decrease the CR is to reduce the amount of CH₄ in the model. A
359 lowering of CH₄ by a factor of 100 (compared to the Moses model) was needed to match the
360 synthetic and observed CR, which does not seem realistic. An other way to adjust the CR is to
361 modify the VER altitude profile. This can be achieved by modifying the hydrocarbon profiles
362 in 4.1.a or by using another profile than the Chapman function defined in equation (3). Many
363 combinations have been tried (lowering or increasing the hydrocarbon density profiles, using
364 Gaussian, generalized Gaussian, asymmetric Gaussian or Epstein profiles), which did not
365 provide a satisfactory result. Finally, we obtained a very good fit of the CR profile by shifting
366 the UVIS observations upward by 125 km, using a Chapman function and the Moses *et al.*
367 (2000) density profiles, without additional modification. In a study of Titan's limb spectra
368 obtained by the Composite InfraRed Spectrometer (CIRS) onboard Cassini, Vinatier *et al.*
369 (2007) showed that an altitude offset corresponding to a spacecraft altitude-control pointing
370 uncertainty of ~2 mrad (Flasar *et al.* 2004) was also required to fit their observations. The 125
371 km offset we need, which corresponds to 0.4 mrad, is therefore well within Cassini pointing
372 uncertainties. Figure 5a shows the shifted UVIS brightness profile in the integrated 1550-
373 1620 Å bandwidth with the best fit in red. The model, calculated every 50 km MRH, has been
374 smoothed over 7 pixels to account for the slit spatial resolution (300 km). The blue points
375 show the 1550-1620 Å brightness before subtraction of the reflected sunlight component and
376 illustrate well the requirement to separate the H₂ from the reflected sunlight components to
377 study the airglow. The effect of the hydrocarbon absorption is illustrated in Fig. 5b, which
378 shows the unsmoothed synthetic brightness, with and without the effect of the hydrocarbon
379 absorption. It is seen that the attenuation is effective below 900 km, with a 50% reduction of

380 the signal at 50 km MRH. The brightness peaks near the homopause level, as already noted by
381 Yelle *et al.* (1986). The best vertical VER displayed in Fig. 5c is a β -Chapman profile,
382 characterized by a maximum value of $0.67 \text{ photons cm}^{-3} \text{ s}^{-1}$ at 1020 km and a scale height of
383 284 km. This solution is not unique, as a range of shape factors can be attributed to the
384 Chapman function. Comparable fits to the 1550-1620 Å brightness have been experimented
385 with a shape factor fixed to 0.5 or varying freely in the regression. In the case of shape factor
386 fixed to 0.5, the best VER is characterized by a maximum of $0.71 \text{ photons cm}^{-3} \text{ s}^{-1}$ at 1000
387 km. When left free, the best shape factor is 2.1, with a maximum of $0.65 \text{ photons cm}^{-3} \text{ s}^{-1}$ at
388 1038 km. Compared to the best β -Chapman, this gives v_m and Z_m variations of 6% and 2%,
389 respectively. The 1550-1620 Å VER can be extended to the entire H₂ UV bands in 800-1650
390 Å by multiplying v_m by 5.27, which is the factor between the integrated intensities in these
391 two bandwidths in the synthetic H₂ airglow spectrum.

392 As mentioned previously, two factors affect the emergent spectra. The first one is the
393 absorption by hydrocarbons which partly attenuates the emission between the emitter and the
394 observer. The second one is the shape of the VER, which puts more or less weight on some
395 portion of the LOS, as illustrated in Fig. 6. Figure 6a shows the average optical depth $\tau(S)$ in
396 the 1150-1650 Å bandwidth for $Z_0=50$ km, while Fig. 6b shows the corresponding VER
397 intercepted by the LOS. It is seen that the unabsorbed emission (black curve) has two separate
398 components. The one with $S<0$ is completely absorbed and does not contribute to the
399 observed emission. As the MRH increases, the two portions of the intercepted VER come
400 near each other and start to merge at ~ 450 km to form a one-block bulk of emission. Figure
401 6c and 6d demonstrate this merging in the case of $Z_0 = 700$ km. The hydrocarbon attenuation
402 is weaker and a substantial portion of the emission at $S<0$ starts to contribute to the total
403 signal. At $Z_0 = 900$ km, the average optical depth is less than unity all along the LOS and the
404 emission in each point contributes to the observed signal. This figure demonstrates that a

405 large increase/decrease of the hydrocarbon number densities may not have a noticeable effect
406 on the emergent brightness. At 50 km MRH for example, a large increase of the hydrocarbon
407 densities will not influence the emission at $S < 0$, as the optical depth is already much larger
408 than unity. This increase would only affect the region where $\tau(s)$ is near unity, i.e. around
409 $S = 7000$ km. As the intercepted VER has a minor contribution in this portion of the LOS, the
410 emergent signal would not be significantly modified.

411 Taking into account the 125 km shift, the lowest probed altitude is -1200 km MRH. As
412 the hydrocarbon density profiles start at -115 km in the Moses *et al.* (2000) model, we need
413 to extend these profiles to lower altitude to examine the full dataset. The Moses hydrocarbon
414 density profiles have been extended to -1200 km by keeping their first value at -115 km
415 constant throughout the lower altitudes until -1200 km. Figure 7 shows a comparison between
416 the observed CR (black curve) and the CR deduced from the best synthetic emergent spectra
417 (red curve). The CR for the unabsorbed synthetic airglow spectrum is 1.5, higher than the 1.1
418 value pointed out for an auroral (i.e. electron impact) H_2 spectrum (Gustin *et al.*, 2006).
419 Starting from the top, it is seen that the synthetic CR is constant at 1.5 between 4000 and 950
420 km, as all spectra are unaffected by hydrocarbons. At 950 km, the modeled CR starts to
421 increase as the hydrocarbon layer is reached. The CR maximizes at 850 km and then
422 decreases at lower altitudes. This effect is due to the intercepted VER, which starts to separate
423 into two components. The emission with $S < 0$ starts to be completely absorbed for all
424 wavelengths, while the emission for $S > 0$ is less and less affected by hydrocarbons, because 1)
425 the path from S to infinity is too short to create a significant optical depth 2) the VER shifts
426 towards the right, i.e. towards lower values of $\tau(s)$, leaving the low altitude emergent spectra
427 practically unabsorbed. In other words, the absorption at low altitude does not affect much the
428 spectral shape of the emergent emission but essentially attenuates the overall integrated
429 brightness by a factor of ~ 2 . Between 4000 and 2500 km MRH, the observed CR are scattered

430 around the theoretical value because of the low S/N ratio. Between 2500 and 1100 km, the
431 observed CR is significantly lower than the theoretical value. This is due to an unidentified
432 feature at 1255 Å peaking in this portion of the atmosphere, which gives more weight to the
433 denominator of the observed CR. Below 1100 km, the synthetic and observed CR fit well
434 down to -500 km, where the observed CR are lower than expected, likely because the low-
435 altitude spectra longward of 1500 Å is strongly influenced by the reflected sunlight emission.
436 This component has been removed from the data, but the residual of the subtraction may lead
437 to a significant uncertainty on the remaining H₂ signal.

438 We experimented other methods to extend the hydrocarbon density profiles to the lower
439 altitudes, basically in lowering the density profiles. As expected, these attempts did not
440 notably change the resulting synthetic CR profiles because of the position of the intercepted
441 VER along the LOS, as discussed before. At this point, a visual comparison between the
442 observed and best synthetic emergent spectra has been performed for all altitude bins. The fits
443 were found very satisfactory in terms of general shape, overall intensity and hydrocarbons
444 absorptions. However, a few individual lines in some best fits were found too intense or too
445 weak depending on the altitude bin examined. This is illustrated in Fig.8a for the emergent
446 spectrum at 300 km, which shows that the overall fit to the data is good, but presents a few
447 over-bright lines at specific wavelengths. Figure 8b shows a comparison between the Hallet *et*
448 *al.* (2005) airglow spectrum used in this study and a laboratory H₂ spectrum obtained from
449 impact of 20 eV electrons (Dziczek *et al.* 2000). It is seen that the main differences between
450 the two spectra are due to several individual lines, and correspond to the discrepant peaks
451 observed in Fig. 8a, as indicated by the arrowed lines. They correspond to H₂ transitions
452 excited by fluorescence and are identified by using Table 2 of Liu and Dalgarno (1996),
453 which lists the principal fluorescence H₂ lines resulting from the absorption of EUV solar

454 radiation obtained from the study of the Jovian airglow. The transitions determined in Fig. 8
455 generally correspond to the most intense fluorescence lines of this table.

456

457 4.3. Electron-impact and fluorescence contributions.

458 The H₂ spectrum from Hallet *et al.* (2005) used in the previous sections represents an
459 average airglow emission and is composed of a fixed combination of electron impact and
460 solar fluorescence excitations. The ratio between the contribution of electron impact and
461 fluorescence on the emergent emission may vary with altitude. In order to evaluate the
462 magnitude of both contribution with MRH, the spectral analysis in the 1150-1650 Å bandpass
463 is performed again here, with the Hallet *et al.* (2005) spectrum replaced by the blending of an
464 e-impact H₂ spectrum obtained in the laboratory and individual fluorescence H₂ lines arising
465 from solar EUV pumping. Two e-impact laboratory spectra at 300 K have been tested. The
466 first one has been obtained from impact of 100 eV electrons (Liu *et al.* 1998) and the second
467 one from 20 eV electrons (Dziczek *et al.*, 2000). The main differences between the 100 eV and
468 20 eV spectra are due to the EF cascade, which populates the B electronic state through
469 E,F¹Σ_g⁺ → B¹Σ_u⁺ transitions. The cascade is enhanced for low energy excitation and
470 maximizes for 20 eV electrons (see Fig. 10 of Ajello *et al.* 2005). This enhancement can be
471 detailed by the examination of a spectrum resulting from the EF cascade process only
472 (without direct excitation), obtained with a time-resolved electron-impact technique (Dziczek,
473 *et al.* 2000). The EF spectrum shows that cascade has emission bands all over the EUV and
474 FUV bandwidth. The cascade process most strongly populates the v=0 vibrational state of B,
475 whereas direct excitation mainly populates v=6, 7 of B. The EF spectrum is more intense in
476 the FUV, with a maximum contribution of the L(0,3) band at 1276Å, L(0,4) at 1335 Å and
477 L(0,5) and 1395 Å, followed by well-defined peaks near 1436, 1458, 1488, 1518, 1546, 1578
478 and 1608 Å.

479 For both e-impact spectrum, an emergent spectrum is calculated for each 50 km
480 altitude bin following equations (1), (2) and (3), with the hydrocarbons from the Moses *et al.* (
481 2000) model and the best VER obtained in the previous paragraph. We add to this spectrum
482 the strongest solar fluorescence lines reported in Table 2 of Liu and Dalgarno (1996). Each
483 line is convolved to the UVIS spectral resolution and is allowed to vary freely in the fitting
484 procedure. Five additional lines have been included in the procedure to improve the fit: Ly- α
485 at 1215.7 Å, the OI triplet at 1302.2, 1304.09 and 1306.0 Å and the mystery feature at 1255
486 Å. The combination of these contributions forms a new synthetic airglow spectrum that is
487 compared to the observed spectra at each MRH. The least-squares regressions have been
488 performed for altitudes from -1200 to 3000 km MRH. The results reveal that the best fits with
489 100 eV and 20 eV spectra are very similar, with a slight preference for the 20 eV spectra. It is
490 however difficult to point out a particular spectral region with systematic improvement,
491 because of all the individual lines varying freely included in the regression. In fact, because of
492 the medium resolution of the data (~ 5.5 Å), some intense pumped H₂ lines included in the
493 regression coincide with lines enhanced by the EF cascade: the 1276 Å line coincides with the
494 pumped lines at 1272.81 Å and 1279.10 Å [L(11,7) R(1)+P(3) from CII and OVI], the 1335 Å
495 line coincide with the 1334.28 Å pumped line [L(5,6) R(1) from CII and OVI] and the 1395 Å
496 line coincide with the pumped 1394.25 Å line [L(11,10) R(1) from Ly- γ]. This means that a
497 specific observed peak enhanced by the EF cascade can be fitted as well with the 20 eV
498 spectrum alone or a combination of the 100 eV spectrum with solar pumped lines. Still, the
499 overall fit with the 20 eV spectrum are found slightly better when compared to the data.
500 Examples of best fits at -700, 50 and 1050 km MRH are shown in Fig. 9. For all spectra, the
501 20 eV electron impact component dominates the total emission, along with a few fluorescence
502 lines. The most intense fluorescence H₂ lines, clearly apparent in Fig. 9, are found at 1265.68
503 Å [L(6,5) P(1)], 1362.04 and 1365.66 Å [L(11,9) P(3) and [L(6,7) P(1)], 1369.0 Å [L(2,5)

504 P(6)], 1461.97 Å [L(6,9) P(1)], 1546.72 Å [L(6,13) P(1)], 1607.50 and 1607.90 Å [L(6,11)
505 P(1)] and [L(5,12) R(1)]. The contribution of the 1255 Å mystery feature is weak for the
506 spectra at -700 and 50 km MRH in Fig. 9 but clearly visible for the 1150 km spectrum. In
507 order to determine the contribution of the different EUV solar lines in the pumping process,
508 the individual H₂ lines due to the same solar source have been added up for each best
509 synthetic spectrum and plotted versus MRH in Fig. 10. This figure also shows the Ly- α line
510 limb profile and presents the contributions of e-impact and fluorescence to the total airglow
511 emission. Some relevant number from the plots in Fig. 10 are tabulated in Table 2. It is seen
512 that the Ly- α line maximizes at 1100 km with 802 R, which corresponds to the altitude of the
513 airglow peak within 50 km (i.e. below the spatial resolution of one UVIS pixel), as already
514 noticed for V1 and V2 limb scans (Yelle *et al.* 1986). The total emission due to fluorescence
515 peaks at 900 km with 1445 R and the emission due to electron impact peaks at 1150 km with
516 2743 R, for a total airglow emission of 3943 R peaking at 1050 km. Taking into account the
517 11 years solar cycle, these numbers can be readily compared to the limb values obtained from
518 the two Voyager encounters with Saturn. The Ly- α line is about two to three times weaker for
519 UVIS compared to Voyager, while the total H₂ emission compares well. The much higher Ly-
520 α brightness observed during the Voyager observations is attributed to the tilted Saturn's rings
521 reflecting a significant amount of emission into the detector, while the rings appeared
522 horizontal during the UVIS observations. Table 2 also gives the intensity of the pumped line
523 used in the analysis of a HUT disk spectrum of the Jovian dayglow (Liu and Dalgarno, 1996),
524 converted to our observation conditions. The Liu and Dalgarno figures have been derived
525 from a disk spectrum and thus cannot be readily compared to ours, which have been obtained
526 from limb-viewing observations. Yet, comparisons between the Liu and Dalgarno values and
527 the UVIS pumped lines brightness averaged from -1200 to 2500 km show that the main
528 contributor to fluorescence for both planets is Ly- β , followed by solar OVI, CII, and NII in

529 that order. The main lines contributing to fluorescence are the L(6,13) P(1) and L(5,12) R(1)
530 transitions at 1607.50 Å and 1607.90 Å respectively. This contribution is clearly seen in the
531 fits presented in Fig. 9. The fits require the addition of the OI triplet at 1304 Å for the low-
532 altitude spectra, and a mystery feature at 1255 Å which peaks at 1200 km. The altitude profile
533 of the 1255 Å line displayed in Fig. 10 looks triangular, quite different from the fluorescence
534 lines. It should be stressed out that the fluorescence lines from Table 2 of Liu and Dalgarno
535 (1996) used in our regression correspond to the main features of the pure fluorescence
536 spectrum. However, they only represent 28% of the total integrated fluorescence spectrum
537 presented in Liu and Dalgarno (1996), as the fluorescence emission exhibits a continuous
538 emission in the UV. If we then multiply the intensity of the pumped lines used in our
539 regression by 3.57 and remove this total fluorescence contribution from the best fits, we find
540 that the electron impact excitation process dominates the emission, with a maximum
541 contribution of 80% at 1400 km and an average contribution of 68% in the -1200 to 2500 km
542 range. The technique we use to evaluate the fluorescence and electron impact contributions to
543 the total airglow should be considered as a first order survey, as it bears two main
544 weaknesses. First, the contribution of the main fluorescence lines listed in Table 2 of Liu and
545 Dalgarno (1996) somewhat depends on the gas temperature and second, we scaled the
546 electron impact spectrum component to the calculated VER and added the fluorescence lines
547 afterwards in the regression, which may lead to an overestimate of the electron impact
548 contribution. On the other hand, the comparison between the e-impact laboratory spectra and
549 the airglow synthetic spectrum from Hallet *et al.* (2005) in Fig. 8 shows that the airglow
550 spectrum can be very well reproduced by combining the e-impact spectra with the
551 fluorescence pumped solar lines. We thus find this method appropriate in our airglow
552 simulations.

553 **5. Conclusions**

554

555 A total of 109 UVIS limb spectra at ~ 5.5 Å resolution of the Kronian airglow,
556 spanning the altitude range -1200 to 4000 km at the tangent point have been analyzed. The
557 limb brightness in the 1150 - 1850 Å range is dominated by Ly- α , peaking at 1100 km MRH
558 with 802 R, reflected sunlight maximizing at -950 km MRH with 16.5 kR and H₂ Lyman and
559 Werner bands which peak at 1050 km MRH with a maximum of 3.9 kR. The UVIS integrated
560 H₂ brightness at the altitude peak compares well with the values obtained with the UVS V1
561 and V2 spectrometers, taking into account the EUV solar flux ratio at the time of the
562 observations. The Ly- α brightness peaks at the same altitude as the H₂ bands, near the
563 homopause level, but our value is significantly lower than the V1 and V2 observations (Yelle
564 *et al.* 1986), probably because of the reflection of interplanetary Ly- α by Saturn's rings, more
565 inclined towards the instrument during the Voyager observations.

566 A model of the airglow emission taking into account hydrocarbon absorption along the
567 LOS has been developed, based on a H₂ synthetic airglow spectrum (Hallet *et al.* 2005) and
568 the Moses *et al.* (2000) model of the Saturn equatorial atmosphere. A vertical profile of the H₂
569 volume emission rate has been derived from fits between the observed and modeled H₂ limb
570 brightness in the 1550 - 1620 Å bandwidth. We find that the best agreement is obtained by
571 shifting the data upward by 125 km, within the pointing uncertainty related to our
572 observations. Our best representation of the vertical volume emission rate is a β -Chapman
573 function which peaks at 1020 km and emits 3.5 photons $\text{cm}^3 \text{s}^{-1}$ in the 800 - 1650 Å bandwidth.
574 The scale height of the Chapman function is 284 km, which is five times the scale height of
575 the neutral atmosphere ($H \sim 53$ km assuming a temperature of 130 K). This result, already
576 pointed out by Yelle *et al.* (1986), shows that the source of excitation extends throughout the
577 entire upper atmosphere of the planet.

578 A comparison between the observed and synthetic spectra has been carried out using a
579 first-order hybrid model of airglow, consisting of a free combination between an electron
580 impact H₂ spectrum and intense fluorescence H₂ lines reported by Liu and Dalgarno (1996).
581 Laboratory spectra excited by 20 eV and 100 eV electrons have been tested. The main
582 differences between these two spectra are due to the EF cascade process, which increases the
583 population of the $v=0$ vibrational level of B and enhances specific H₂ emitted lines. This
584 effect is maximum for 20 eV electrons and is used to discriminate between 20 eV and 100 eV
585 spectra. However, the spectral lines enhanced by cascade coincide with fluorescence lines,
586 which makes it difficult to choose between the modeled emergent spectra obtained with the
587 20eV and 100 eV spectra. Nevertheless, the emergent synthetic airglow spectra built with the
588 20 eV spectrum provided overall better fits to the observations. This suggests that the airglow
589 is principally due to low-energy photoelectrons, as was already suggested by the study of the
590 Jovian UV airglow by Liu and Dalgarno, (1996). The photoelectron flux spectrum they
591 derived from XUV solar excitation had energies mostly lower than 60 eV, with an average of
592 33 eV and a peak at 25 eV. We find that electron impact process dominates Saturn's airglow
593 emission, with an average contribution of ~ 68% in the -1200 to 2500 km MRH range.

594 This study provides the first study of recent UV spectra of the Kronian airglow, which
595 is scarcely described in the literature. A next step in the study of airglow would be to use a
596 self-consistent spectral model of H₂, based on the incident XUV and EUV solar flux. This
597 would help to univocally determine 1) the mean energy of the photoelectrons responsible of
598 the airglow, 2) the relative contribution of photoelectron and fluorescence excitation to the
599 total emission and 3) that the airglow at Saturn, as for Jupiter, can be solely attributed to solar
600 fluorescence and photoelectron excitation without the need of an additional energy source.

601

602

603 Acknowledgements

604 The PRODEX program of ESA provided financial support for this research. J.-C.G.

605 acknowledge support from the Belgian Fund for Scientific Research (contract NAS5-32985).

606 This work is supported by the Cassini Project.

607

ACCEPTED MANUSCRIPT

608

609 **References**

610

611 Ajello, J. M., Srivastava, S. K., Yung, Y. L., 1982. Laboratory studies of UV emissions of H₂
612 by electron impact - The Werner- and Lyman-band systems, *Phys. Rev.*, 35, 2485-2498.

613

614 Ajello, J. M., W. Pryor, L. Esposito, I. Stewart, W. McClintock, J. Gustin, D. Grodent, J.-C.
615 Gérard, J.T. Clarke, 2005. The Cassini Campaign observations of the Jupiter aurora by the
616 Ultraviolet Imaging Spectrograph and the Space Telescope Imaging Spectrograph, *Icarus*,
617 178, 327-345, doi:10.1016/j.icarus.2005.01.023.

618

619 Ajello, J. M., Gustin, J., Stewart, A. I. F., Larsen, K., Esposito, L., Pryor, W., McClintock,
620 W., Stevens, M. H., Malone, C. P., Dziczek, D., 2008. Titan airglow spectra from the Cassini
621 Ultraviolet Imaging Spectrograph: FUV disk analysis, *Geophys. Res. Lett.*, 35, L06102,
622 doi:10.1029/2007GL032315.

623

624 Broadfoot, A.L., Sandel, B.R., Shemansky, D.E., Holberg, J.B., Smith, G.R., Strobel, D.F.,
625 McConnell, J.C., Kumar, S., Hunten, D.M., Atreya, S.K., Donahue, T.M., Moos, H.W.,
626 Bertaux, J.L., Blamont, J.E., Pomphrey, R.B., Linik, S., 1981. Extreme ultraviolet
627 observations from Voyager 1 encounter with Saturn, *Science*, 212, 206.

628

629 Broadfoot, A. L. and 18 co-authors, 1986. Ultraviolet Spectrometer Observations of Uranus,
630 *Science*, 233, 74-79, doi: 10.1126/science.233.4759.74.

631

632 Chen, R. H., 1981. Studies of Jupiter's lower ionospheric layers, *J. Geophys. Res.*, 86, 7792-
633 7794

634

635 Clarke, J.T., Hudson, M. K., Yung, Y. L., 1987. The excitation of the far ultraviolet
636 electroglow emissions on Uranus, Saturn, and Jupiter, *J. Geophys. Res.*, 92, 15139-47.

637

638 Cravens, T. E., Victor, G. A., and Dalgarno, A., 1975. The absorption of energetic electrons
639 by molecular hydrogen gas, *Planet. Space Sci.*, 23, 1059.

640

641 Dziczek, D., Ajello, J. M., James, G. K., Hansen, D. L., 2000. Cascade contribution to the H₂
642 Lyman band system from electron impact, *Phys. Rev.*, 61, id 064702, doi :
643 10.1103/PhysRevA.61.064702.

644

645 Esposito, L., and 18 colleagues, 2004. The Cassini Ultraviolet Imaging Spectrograph
646 investigation, *Space Science Rev.*, 115, 299.

647

648 Flasar, F. M. and 44 co-authors, 2004. Exploring the Saturn system in the thermal infrared:
649 The composite infrared spectrometer. *Space Sci. Rev.* 115, 169–297.

650

651 Gustin, J., Gérard, J.-C., Grodent, D., Cowley, S.W.H., Clarke, J.T., Grard, A., 2004. Energy
652 – flux relationship in the FUV Jovian aurora deduced from HST-STIS spectral observations,
653 *J. Geophys. Res.*, 109, doi:10.1029/2033JA010365.

654

655 Gustin, J., Cowley, S.W.H., Gérard, J.-C., G. R., Gladstone., Grodent, D. and Clarke, J.T.,
656 2006. Characteristics of Jovian morning bright FUV aurora from Hubble Space

- 657 Telescope/Space Telescope Imaging Spectrograph imaging and spectral observations, J.
658 Geophys. Res., 111, doi:10.1029/2006JA011730
659
- 660 Gustin, J.; Gérard, J.-C., Pryor, W., Feldman, P. D., Grodent, D., Holsclaw, G., 2009.
661 Characteristics of Saturn's polar atmosphere and auroral electrons derived from HST/STIS,
662 FUSE and Cassini/UVIS spectra, Icarus, 200, 176-187, doi: 10.1016/j.icarus.2008.11.013.
663
- 664 Hallett, J.T., Shemansky, D.E., Liu, X., 2005. A Rotational-Level Hydrogen Physical
665 Chemistry Model for General Astrophysical Application. ApJ. 624, 448-461.
666
- 667 Liu, W., Dalgarno, A., 1996. The ultraviolet spectrum of the Jovian dayglow, ApJ. 462, 502-
668 518
669
- 670 Liu, X., Shemansky, D. E., Ahmed, S. M., James, G. K., Ajello, J. M., 1998. Electron-impact
671 excitation and emission cross sections of the H₂ Lyman and Werner systems, J. Geophys.
672 Res., 103, 26739-26758, doi : 10.1029/98JA02721.
673
- 674 Moses, J.I., Bézard, B., Lellouch, E., Feuchtgruber, H., Gladstone, G.R., Allen, M., 2000.
675 Photochemistry of Saturn's atmosphere I. Hydrocarbon chemistry and comparisons with ISO
676 observations, Icarus, 143, 244-298.
677
- 678 Prangé, R., 1986. New evidence for the role of photoelectrons in the H₂-dayglow of the giant
679 planets, Astron. and Astrophys., 161, no. 1, L1-L4.
680

- 681 Sada, P. V., Bjoraker, G. L., Jennings, D. E. Romani, P. N. McCabe, G. H., 2005.
682 Observations of C₂H₆ and C₂H₂ in the stratosphere of Saturn, *Icarus*, 173, 499-507, doi:
683 10.1016/j.icarus.2004.08.006.
- 684
- 685 Shemansky, D.E., Ajello, J.M., 1983. The Saturn spectrum in the EUV: Electron excited
686 hydrogen, *J. Geophys. Res.*, 88, 459.
- 687
- 688 Smith, G. R., Shemansky, D. E., Holberg, J. B., Broadfoot, A. L., Sandel, B. R., McConnell,
689 J. C., 1983. Saturn's upper atmosphere from the Voyager 2 EUV solar and stellar occultations,
690 *J. Geophys. Res.*, 88, 8667-8678.
- 691
- 692 Stevens, M. H., Gustin, J., Ajello, J. M., Evans, J. S., Meier, R. R., Stephan, A. W., Stewart,
693 A. I. F., Larsen, K., Esposito, L. W., McClintock, W. E., 2010. The Production of Titan's Far
694 Ultraviolet Nitrogen Airglow, submitted to *JGR*.
- 695
- 696 Strobel, D. F., 1979. The ionospheres of the major planets, *Reviews of Geophys. and Space*
697 *Phys.*, 17, 1913-1922
- 698
- 699 Vinatier, S. and 10 co-authors, 2007. Vertical abundance profiles of hydrocarbons in Titan's
700 atmosphere at 15° S and 40° N retrieved from Cassini/CIRS spectra, *Icarus*, 188, 120-138,
701 doi:10.1016/j.icarus.2006.10.031.
- 702
- 703 Wallach, D., Hapke, B., 1985. Light scattering in a spherical, exponential atmosphere, with
704 applications to Venus, *Icarus*, 63, 354-373, doi: 10.1016/0019-1035(85)90052-1
- 705

- 706 Woods, T. N., Eparvier, F. G., Bailey, S. M., Chamberlin, P. C., Lean, J., Rottman, G. J.,
707 Solomon, S. C., Tobiska, W. K., Woodraska, D. L., 2005. Solar EUV Experiment (SEE):
708 Mission overview and first results, *J. Geophys. Res.*, 110, A01312,
709 doi:10.1029/2004JA010765.
- 710
- 711 Yelle, R. V., Sandel, B. R., Shemansky, D. E., Kumar, S., 1986. Altitude variation of EUV
712 emissions and evidence for proton precipitation at low latitudes in the Saturnian atmosphere,
713 *J. Geophys. Res.*, 91, 8756-8770.
- 714
- 715 Yelle, R. V., Sandel, B. R., Broadfoot, A. L., McConnell, J. C., 1987. The dependence of
716 electroglow on the solar flux, *J. Geophys. Res.*, 92, 15110-15124.
- 717
- 718 Yelle, R. V., 1988. H₂ emissions from the outer planets, *Geophys. Res. Lett.*, 15, 1145-1148.
- 719

720 **Tables**

721

722 Table 1: overview of the UVIS limb scan dataset

723

	Start time	Number of records	Integration per record (s)	Mean latitude, longitude (deg)	Mean incidence angle (deg)	Mean phase angle (deg)
1	Oct. 29 2005 19:27:45	4	120	-17, 26.5	23	68
2	Oct. 29 2005 19:35:33	77	30	3-16.5, 35	17	73
3	Nov. 27 2005 08:57:53	7	75	-17.5, 133.5	9	79
4	Nov. 27 2005 09:07:07	68	18	-18, 140	7	81
5	Nov. 27 2005 13:17:55	7	75	-17.5, 227.5	40	125
6	Nov. 27 2005 13:27:07	88	18	-18, 238	44	128

724

725

726

727

728

729

730

731

732

733

734

735

736

737

738

739 Table 2: Characteristics of the main contributions to the airglow emission.

Emission	Peak limb brightness from UVIS (R) ⁶	Peak altitude (Km)	Main H ₂ line contributing	Average brightness from – 1200 to 2500 km MRH (R)	Disk values from Liu and Dalgarno, 1996 (R) ⁷	Peak limb values from V1 and V2 (R) ⁸
H Ly- α	802	1100	-	441		V1: 1936, 2543, V2: 1845
L(6,x) ¹ P(1) from H Ly- β	120	1000	L(6,11) P(1) at 1546 Å	42	9.2	
L(11,x) ² R(1) + P(3) from H Ly- γ	13	750	L(11,7) P(3) at 1279 Å	6	2.8	
L(2,x) ³ R(4) + P(6) from NII	35	900	L(2,10) R(4) at 1623 Å	15	3.1	
W(1,x) ⁴ Q(3) from NII & OVI	26	1250	W(1,5) Q(3) at 1208 Å	10	2.2	
L(5,x) ⁵ R(1) + P(3) CII & OVI	60	900	L(5,11) P(3) at 1613 Å	18	7.1	
1607 Å from H Ly- β , CII & OVI	137	950	L(6,13) P(1) and L(5,12) R(1)	33	8.1	
1255 Å mystery feature	18	1200	-	7		
OI triplet	6	-1000	-	4		
Total H ₂ bands from e ⁻ impact	2743	1150	-	1054	131 ⁹	
Total H ₂ bands from fluorescence	1445	900	-	460	173 ⁹	
Total H ₂	3943	1050	-	1514	304 ⁹	V1: 5386, 4787; V2: 3075

740

741 1. x = 3, 5, 7, 9, 11, 12, 13, 14. L stands for Lyman and W for Werner bands.

742 2. x = 5, 7, 9, 10, 14

743 3. x = 1, 2, 5, 8, 9, 10

744 4. x = 4, 5

745 5. x = 3, 5, 6, 8, 10, 12

- 746 6. Value deduced from the fits in the 1150-1650Å bandwidth. The total H₂ value must be multiplied by 1.33 to obtain the total H₂ brightness in
747 the 800-1650 Å range, giving 5244 R. The V1 and V2 limb values in Yelle *et al.* (1986) refer to “total H₂ bands intensity” without specifying a
748 unambiguous spectral range, which makes it difficult to compare the UVIS and Voyager numbers.
- 749 7. Values from fluorescence lines listed in Table 2 of Liu and Dalgarno, (1996), adapted to Saturn at solar minimum. A factor 0.295 is applied to
750 convert the solar irradiance from Jupiter to Saturn and a conversion factor 0.44 is used to account for the solar activity variation between Dec
751 1990 (HUT) and Nov 2005 (UVIS)
- 752 8. Values from Yelle *et al.* (1986), adapted to Nov 2005 solar activity. A factor of 0.44 and 0.41 is applied to convert from V1 to UVIS and V2 to
753 UVIS, respectively. Two values are associated with V1 because two limb scans have been performed.
- 754 The V1 Ly-a values have been multiplied by 0.68 to take into account the UVS damages during the Jupiter encounter (Ben Jaffel *et al.* 1995).
- 755 9. According to Liu and Dalgarno, (1996), the solar fluorescence on Jupiter contributes 57% of the total observed dayglow emission.
- 756
- 757

758

759

760

761

762 **Figure captions**

763 **Figure 1:** a) Projection of the UVIS slit for the limb viewing observation obtained on 29
764 October 2005 (case 1 in Table 1), showing the four records of the sequence. The long side of
765 the slit represents the 64 spatial pixels of the aperture. A FUV spectrum is associated with
766 each spatial pixel.

767 b) Viewing geometry for a given impact parameter Z_0 (minimum ray height).
768 The observed brightness $B(Z_0)$ is the sum of the $v(S)$ intercepted along the line of sight and
769 attenuated by $\tau(S)$ (equations (1), (2) and (3) within the text).

770

771 **Figure 2:** a) All the raw UVIS spectra have been summed into 50 km altitude bins. The
772 few examples shown here indicate that the emission longward of 1550 \AA is dominated by
773 solar reflectance for the low altitude spectra (-1325 to 625 km). The H_2 bands prevail from
774 625 to ~3000 km. The emission above ~3000 km has a very low S/N ratio and is considered
775 as background. The baseline of each spectrum has been incremented for better legibility.

776 b) Examples of integrated limb brightness profiles for different spectral ranges.
777 The observed solar reflected emission in the 1700-1880 \AA range maximizes at -950 km MRH
778 with 16.5 kR, while the total H_2 bands reach a maximum brightness at 1050 km MRH. In
779 particular the ratio of the 1550-1620 \AA and 1230-1300 \AA bandwidth defines the color ratio
780 and indicates a strong absorption by CH_4 shortward of 1400 \AA .

781

782 **Figure 3:** Comparison between the UVIS spectra at -1025 and 525 km MRH and a
783 model that includes H_2 and solar reflected emissions. The best synthetic solar reflected
784 component is then subtracted from all spectra in order to study the H_2 airglow. These two

785 examples illustrate well the dominance of solar reflection at low altitudes (-1025 km
786 spectrum) and the increase of the H₂ component at higher altitudes (525 km spectrum). Error
787 bars due to the count statistics are shown at 1765 Å.

788 **Figure 4:** Mixing ratio profiles of the two main absorbing species obtained from the best
789 fits to the reflected sunlight component between 1500 Å and 1880 Å (solid lines). The
790 acetylene (C₂H₂) and ethane (C₂H₆) mixing ratios from the Moses *et al.* (2000) model,
791 averaged along the line of sight, are shown in dashed lines. The various symbols indicate
792 abundances derived from recent observation (adapted from Figure 6 of Sada *et al.* 2005). The
793 error bars reflect the uncertainties in abundances and pressure levels.

794

795 **Figure 5:** a) Best fit to the observed integrated brightness in the 1550-1620 Å range with
796 a Chapman function, following equations (1), (2) and (3) listed in paragraph 4.1. The modeled
797 brightness, calculated every 50 km, has been smoothed over 7 pixels to take into account the
798 spatial extend one UVIS pixel during the observations. The blue squares display the 1550-
799 1620 Å raw profile before the removal of the reflected sunlight component, demonstrating the
800 importance of this step in the analysis.

801 b) Best synthetic brightness in the 1550-1620 Å bandwidth, unsmoothed, with
802 and without the attenuation by hydrocarbons. It is seen that the signal peaks near the
803 homopause level and is attenuated for MRH below ~900 km.

804 c) Best β -Chapman vertical profile derived from the fit to the 1550-1620 Å
805 limb brightness. This shows that the emission extends throughout the entire upper atmosphere
806 of Saturn. The listed v_m must be multiplied by 5.27 to extrapolate to the total UV H₂ bands in
807 the 800-1650 Å bandwidth.

808

809 **Figure 6:** Examples of the VER intercepted along the LOS and mean optical depth in the
810 1150-1650 Å bandwidth for two impact parameters. At low altitude, the emission consists of
811 two separated contributions (black curve in panel a), to be multiplied by the cumulated optical
812 depth from each point S to infinity (panel b) The red curve in panel b corresponds to the
813 resulting observed emergent emission. At higher altitudes (panels c and d), the two
814 intercepted VER merge and are more sensitive to the optical depth near S=0.

815

816 **Figure 7:** Color ratio between the integrated brightness in the 1550-1620 Å and 1230-
817 1300 Å bandwidths, illustrating the effect of the CH₄ absorption. The light orange curve
818 shows the synthetic CR obtained before the altitude shift of the observations (see text), and
819 the red curve shows the best synthetic CR obtained after the offset.

820

821 **Figure 8:** a) Example of fit of the airglow emission with the model described in section
822 4.2. which includes the modeled airglow spectrum of H₂ (fluorescence and electron impact) as
823 described by Hallet *et al.* (2005) and the HLyman- α line.

824 b) Comparison between the modeled airglow H₂ spectrum from Hallet *et al.*
825 (2005) and the laboratory H₂ spectrum obtained from impact with 20 eV electrons from
826 Dziczek *et al.* (2000). Most of the discrepancies found in Figure 8a are due to the
827 fluorescence lines, clearly apparent in Figure 8b (lines with arrows). See text for details.

828

829 **Figure 9:** Examples of best fit to the H₂ airglow emission, for three altitude bins,
830 obtained from the combinations of a 20 eV electron impact spectrum and individual H₂
831 fluorescence lines. It is seen that the electron impact component dominates the spectra. The
832 main contributions of fluorescence correspond to the L(6,13) P(1) and L(5,12) R(1)

833 transitions at 1607.50 Å and 1607.90 Å respectively. A mystery line is added to the regression
834 at 1255 Å. Its effect on the best fit is clearly seen in the 1150 km spectrum.

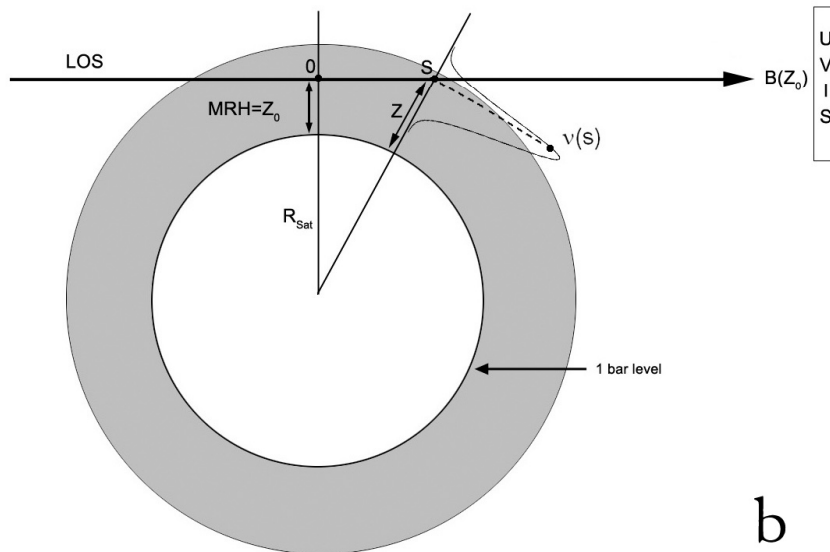
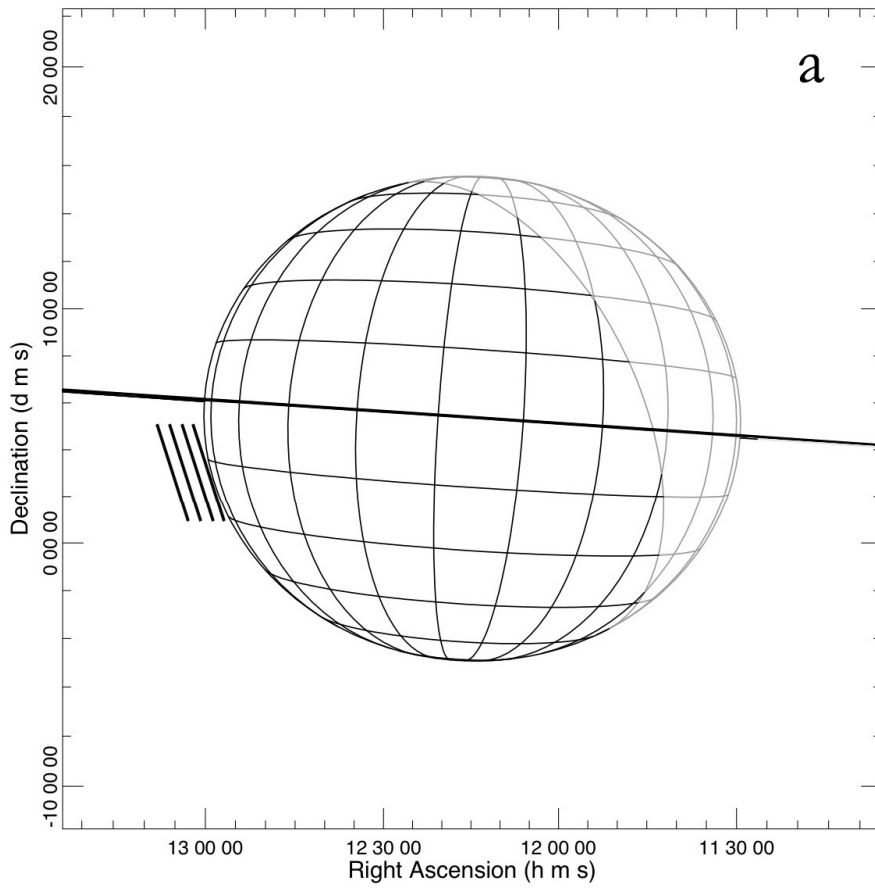
835

836 **Figure 10:** Limb brightness profiles of the main contributors to the H₂ airglow emission in
837 the 1150-1650 Å spectral window, derived from the best fits to the emergent spectra All plots
838 except the H₂ brightness and electron impact contribution plots are smoothed over 5 points. A
839 detailed description is provided in Table 2 and within the text.

840

ACCEPTED MANUSCRIPT

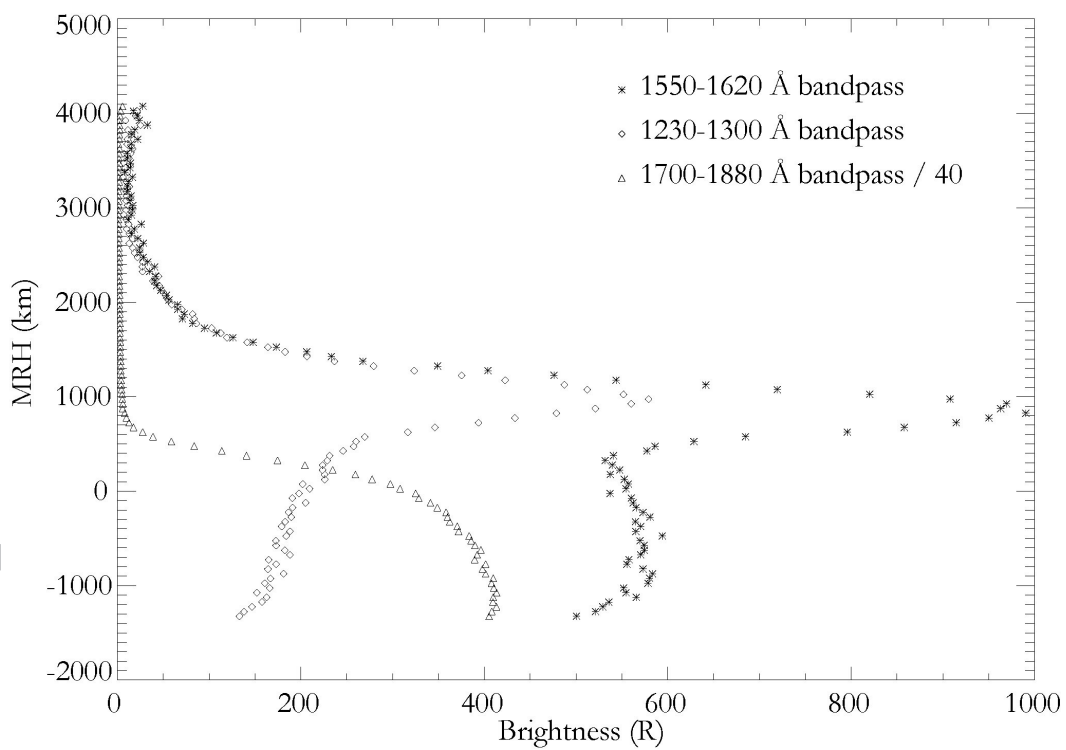
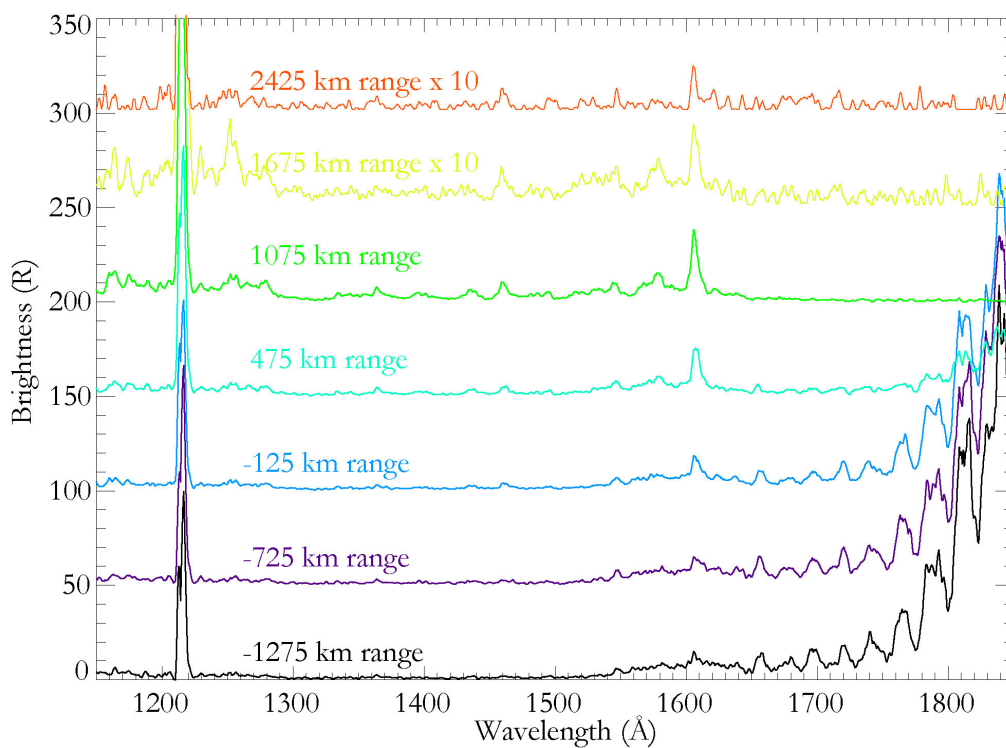
841 Figures



842

843 Figure 1

844

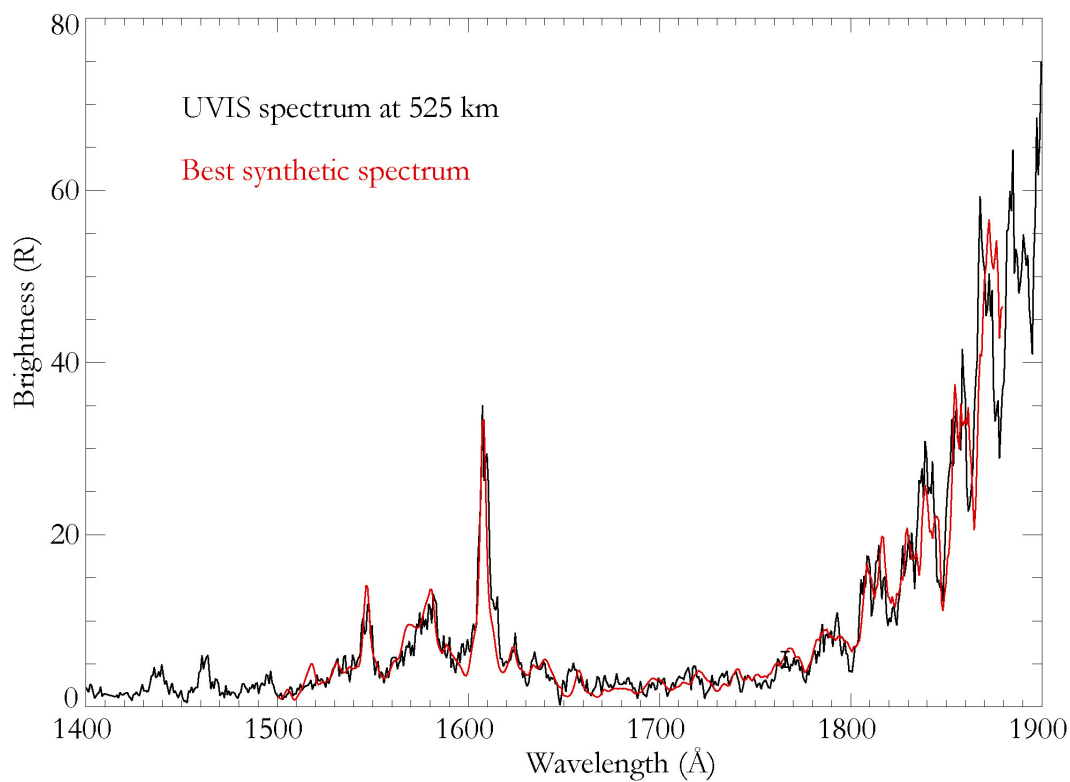
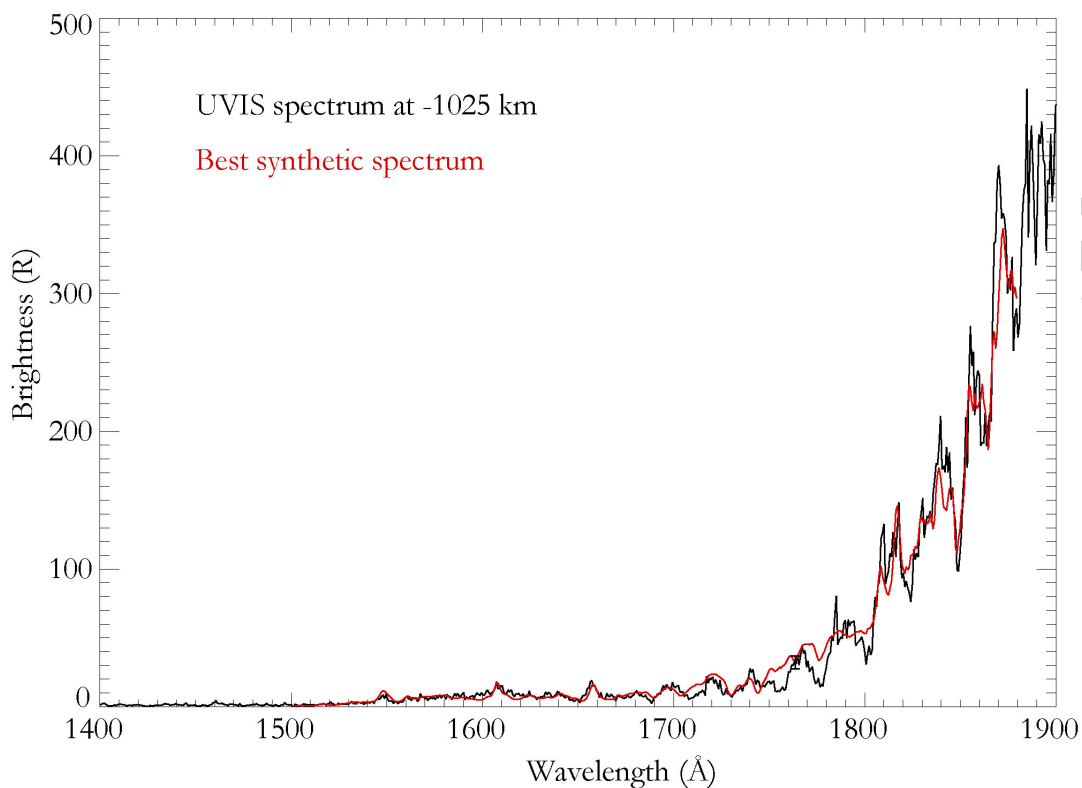


845

846

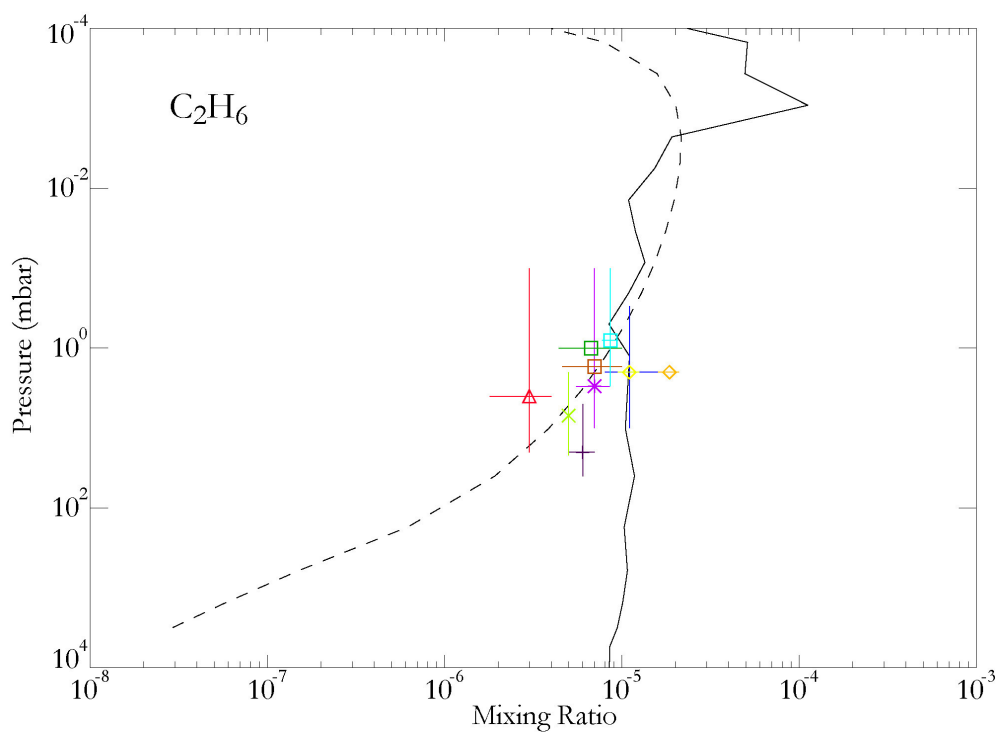
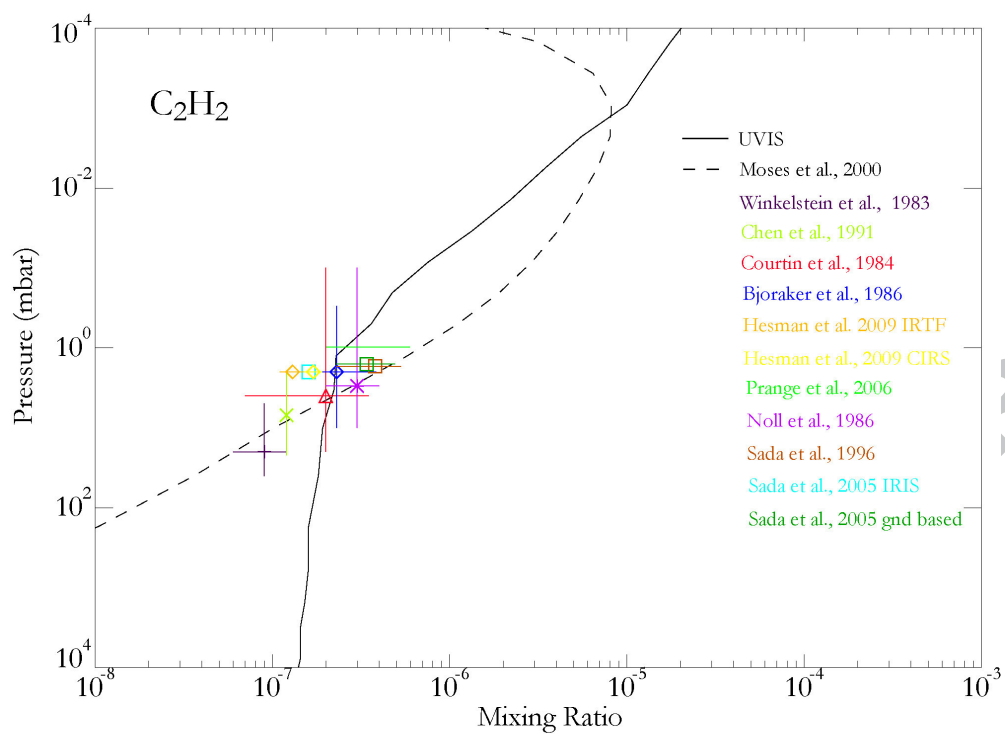
847 Fig. 2

848



849

850 Fig. 3

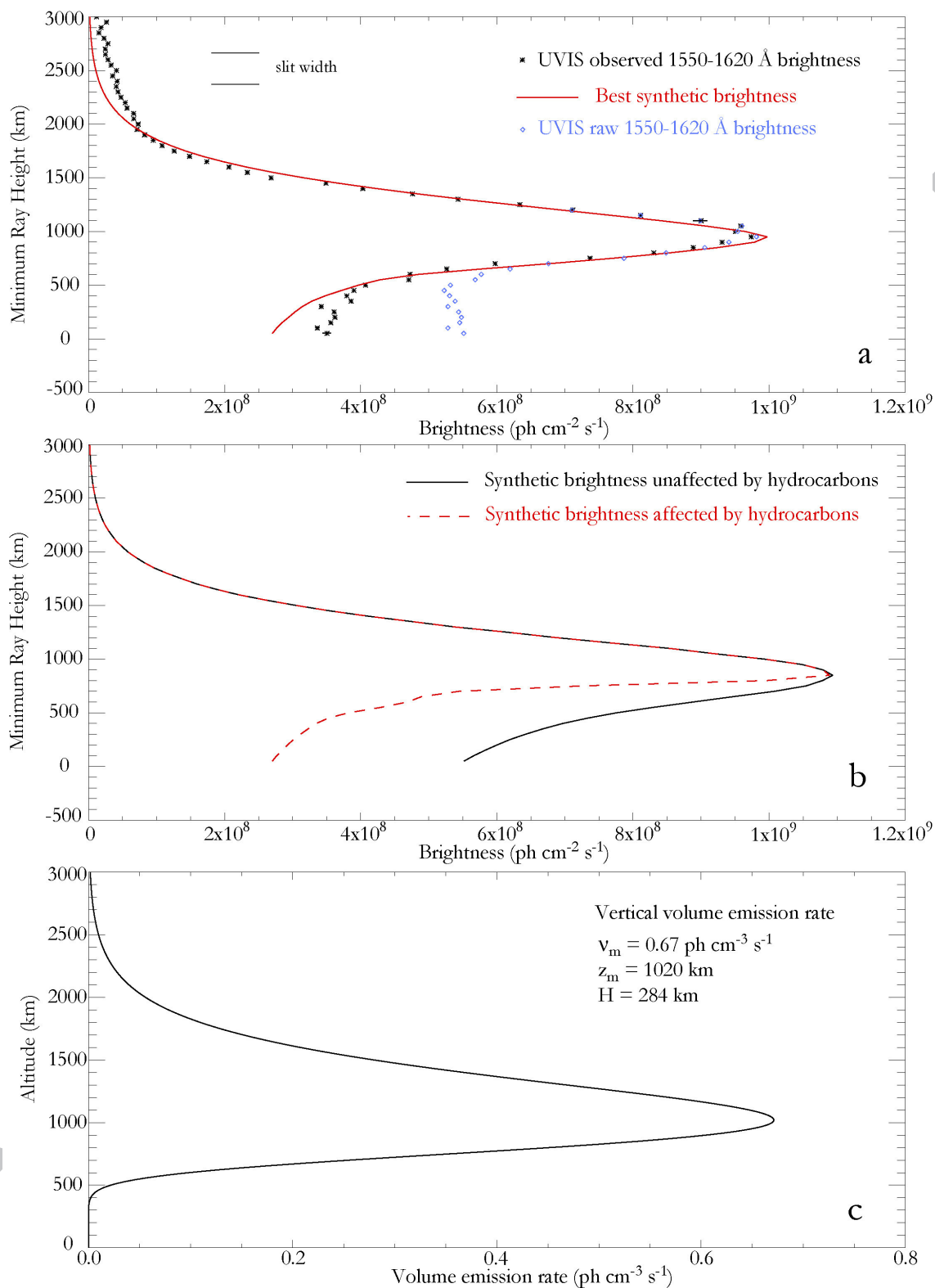


851

852

853 Fig. 4

854

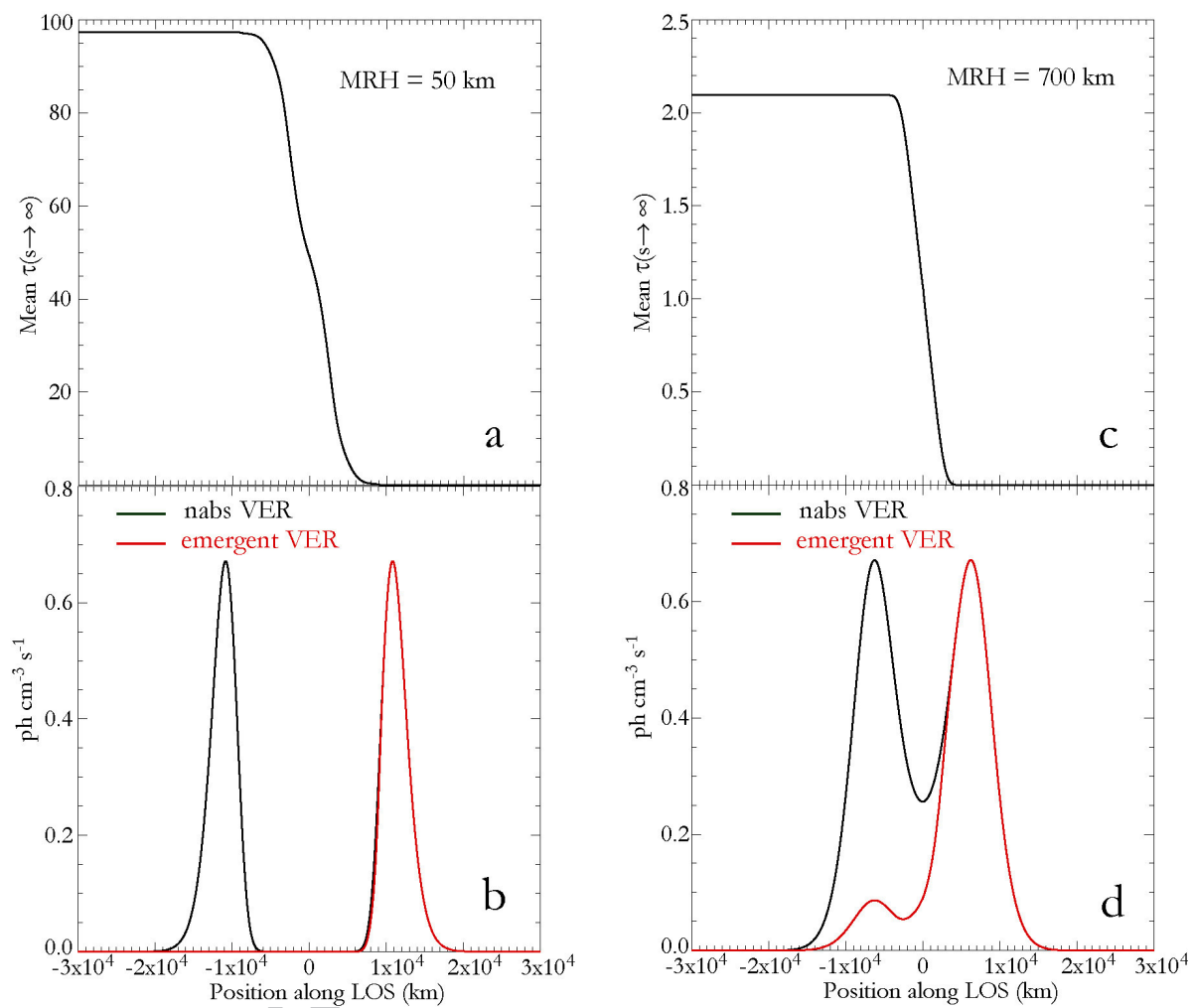


855

856

857 Figure 5

858



859

860

861 Figure 6

862

863

864

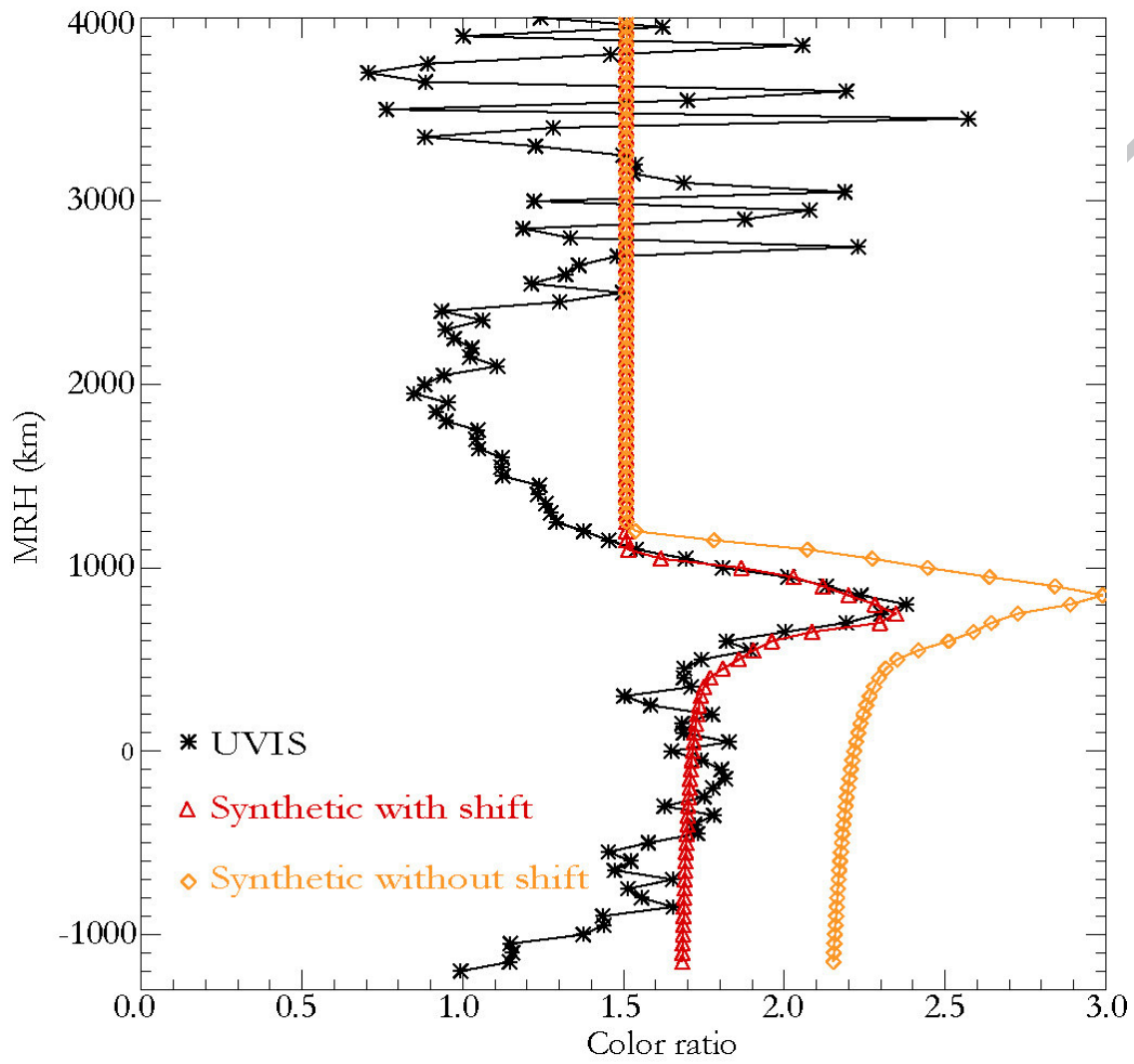
865

866

867

868

869



870

871

872 Figure 7

873

874

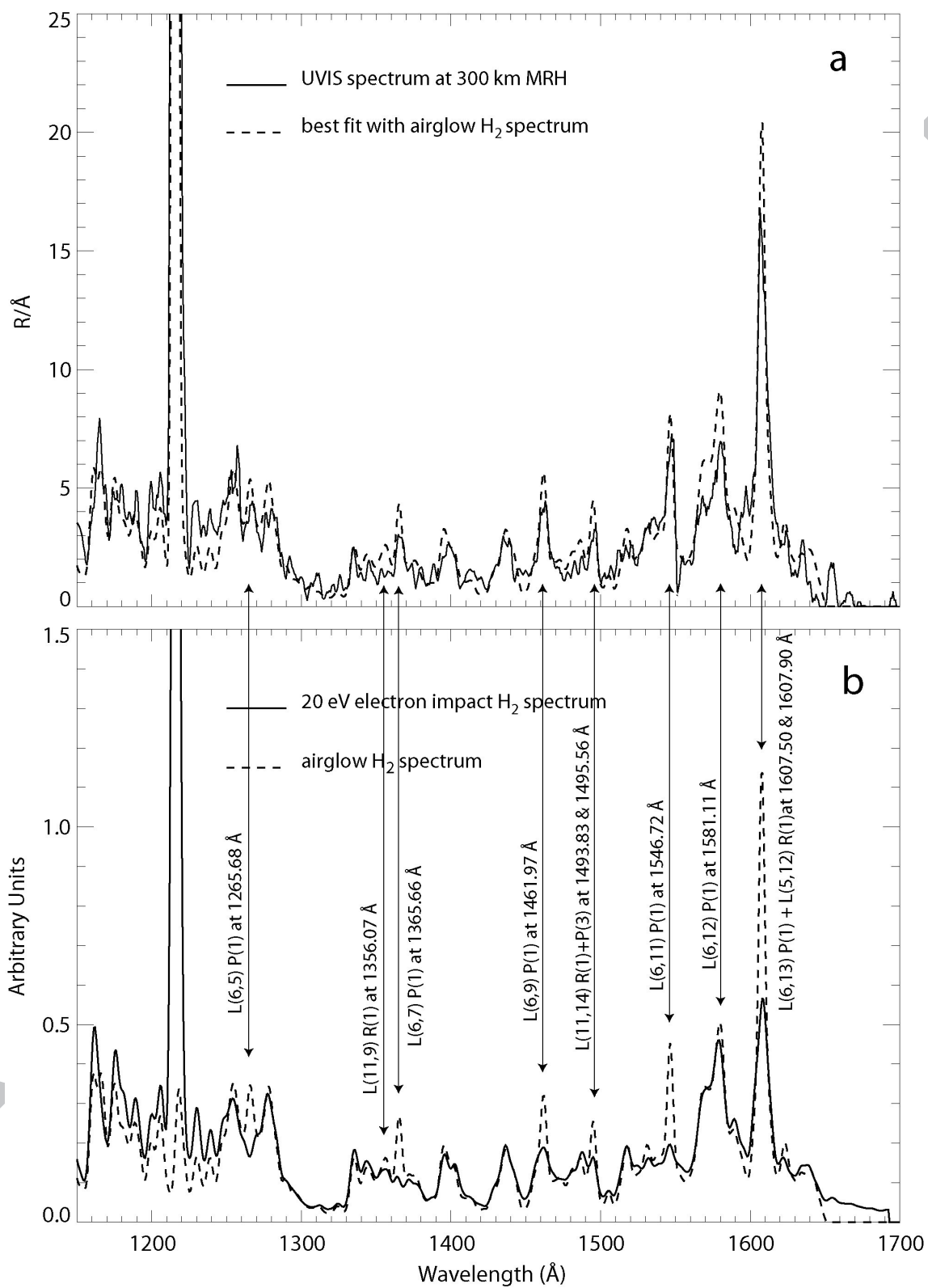
875

876

877

878

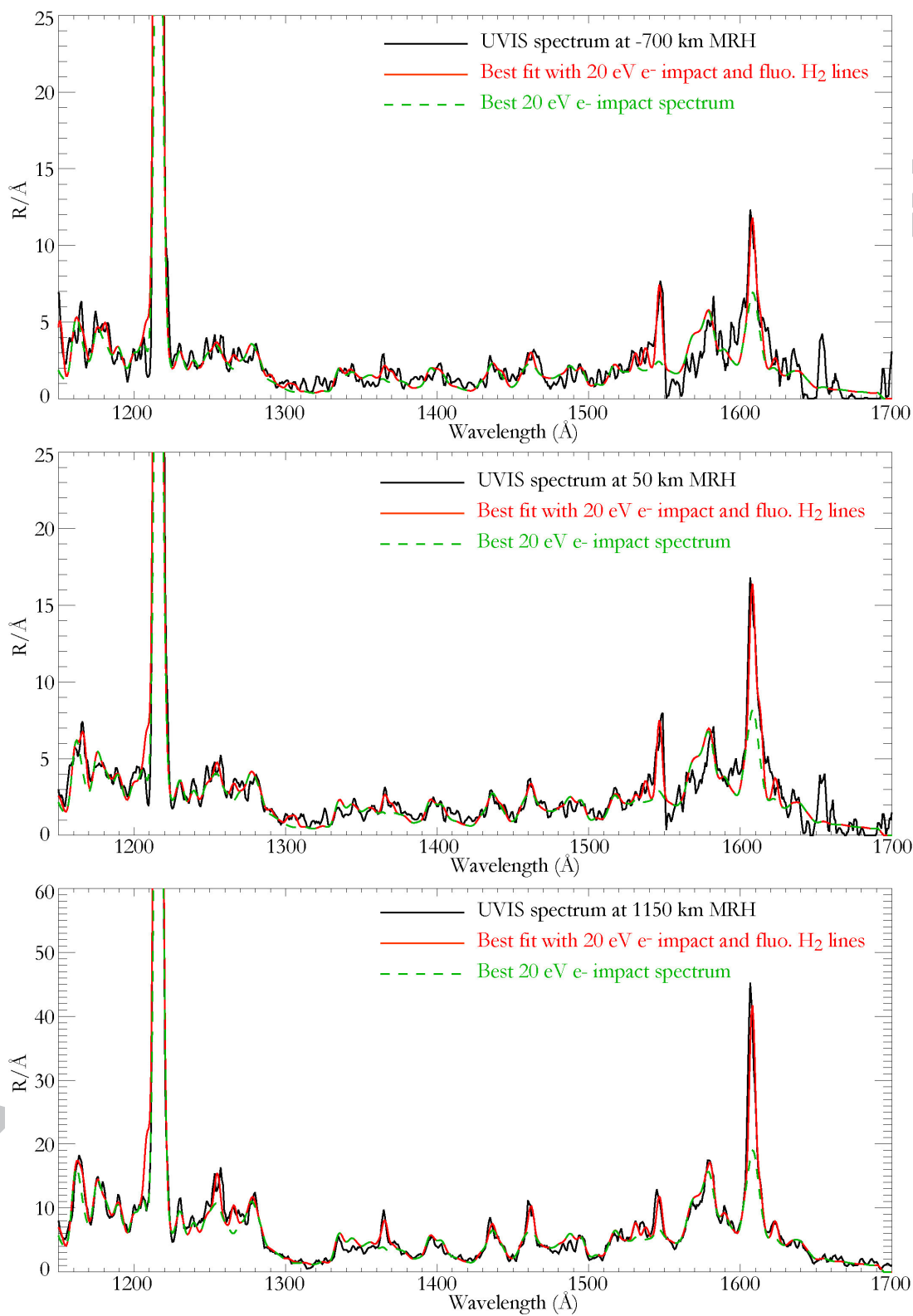
879



880

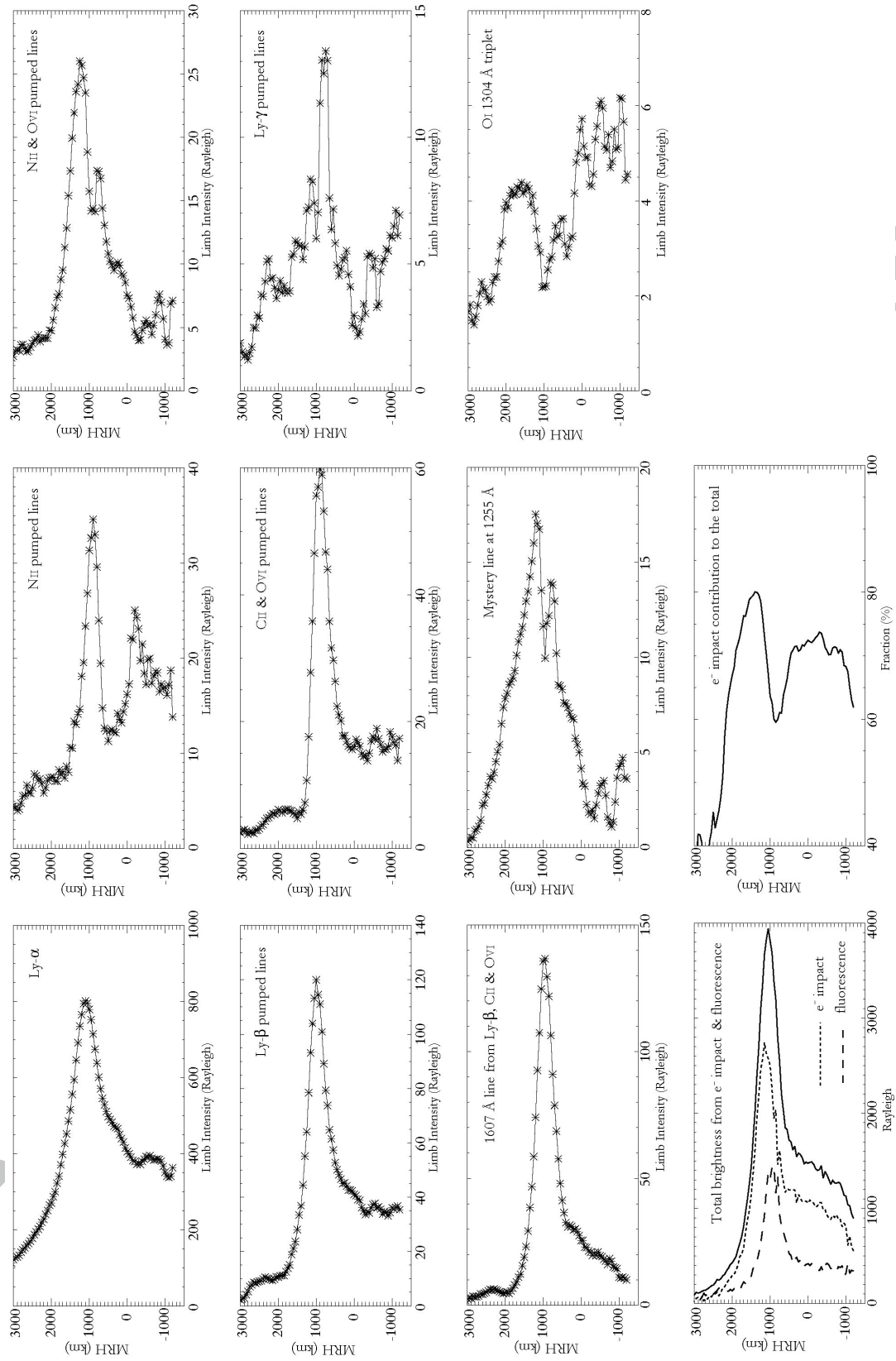
881 Figure 8

882



883

884 Figure 9



885

886 Figure 10